

Sensor-driven autonomous underwater inspections: A receding-horizon RRT-based view planning solution for AUVs

Leonardo Zacchini^{1,2}  | Matteo Franchi^{1,2}  | Alessandro Ridolfi^{1,2} 

¹Department of Industrial Engineering (DIEF), University of Florence, Florence, Italy

²Interuniversity Center of Integrated Systems for the Marine Environment (ISME), University of Genova, Genova, Italy

Correspondence

Leonardo Zacchini, Department of Industrial Engineering (DIEF), University of Florence, via di Santa Marta 3, 50139 Florence, Italy.
Email: leonardo.zacchini@unifi.it

Funding information

H2020 EUMarineRobots,
Grant/Award Number: 731103

Abstract

Autonomous Underwater Vehicles (AUVs) are used by the scientific community for various applications, from collecting well-distributed high-quality data to mapping the seafloor or exploring unknown areas. Nonpredictable environmental conditions and sensor acquisitions make the design of AUV surveys challenging even for expert operators. Multiple attempts are required, and the collected data quality is not guaranteed: The AUV passively stores the sensors' acquisitions that are then analyzed offline after its recovery. In Forward-Looking SONAR (FLS) seabed inspections, the vehicle follows lawnmower paths designed by an expert operator that considers the sensor characteristics. The performance of FLSs is affected by several environmental conditions and possible protruding objects. This paper presents a probabilistic framework for FLS-based seabed inspections that endow the AUV with the ability to autonomously conducting the survey and ensure adequate coverage of the target area. A three-dimensional probabilistic occupancy mapping system for FLS reconstructions to update the covered area map was developed. The map is used by the Coverage Path Planning (CPP) algorithm to evaluate the visibility of the viewpoints that are generated as nodes of a random tree. The Next-Best Viewpoint (NBV) is selected as the first node in the branch expected to collect more data, and the path to reach the NBV is computed using the rapidly exploring random tree (RRT*) algorithm. The sensor-driven coverage approach is used in a receding-horizon manner. The proposed Receding-Horizon Coverage Approach was validated with simulations and real prerecorded data. Finally, the framework was used online during an experimental campaign where several FLS seabed inspections were performed.

KEYWORDS

autonomous navigation 3D occupancy mapping, autonomous underwater vehicle, exploration, forward-looking SONAR, marine robotics, planning

This is an open access article under the terms of the Creative Commons Attribution License, which permits use, distribution and reproduction in any medium, provided the original work is properly cited.

© 2022 The Authors. *Journal of Field Robotics* published by Wiley Periodicals LLC

1 | INTRODUCTION

The last two decades of mobile robotics developments have been led by the increasing demand of scientists, researchers, and industries for intelligent robots to perform complex tasks and acquire data in hazardous scenarios. In marine applications, marine biologists, archeologists, and geologists have sought systems to expand their ability to discover and observe the oceans. Autonomous Underwater Vehicles (AUVs) can carry a wide variety of exteroceptive sensors, ranging from high-resolution MultiBeam Echosounders (MBESs) to Side Scan SONARs (SSSs), Forward-Looking SONARs (FLSs), SubBottom Profilers (SBPs), optical cameras, and so on. Thus, they met field specialists' requirements and have become fundamental tools for collecting high-quality data to study and understand complex and dynamic underwater environments.

Consequently, the scientific community has extensively used AUVs endowed with different payload sets in various applications in the last years (Wynn et al., 2014). In Larroque et al. (2011), the authors used an AUV to collect MBES data to characterizing the active tectonic and gravitational deformation of the northern Ligurian margin, Italy. To identify mechanisms related to the detachment fault denudation at the seafloor and investigate the relation between the mass wasting and the tectonic extension, the authors in Escartín et al. (2017) used the collected micro bathymetric data and geologic samples acquired by an AUV and a remotely operated vehicle (ROV), respectively. MBES data acquired by the Eagle Ray AUV were used in the research work presented in Mitchell et al. (2018). In detail, the MBES data set was used to locate and map the hydrocarbon seeps that are evident in the MBES measurements in Green Canyon Block 600 in the Gulf of Mexico. For deep-ocean seafloor investigations, 6000 m depth rated AUVs acquired MBES, SSS, and SBP data as reported in Caress et al. (2008) and Lee and "Tony" George (2004). The collected data allowed geoscientists to analyze the seafloor morphology, the bathymetric changes associated with sediment transport, gravitational driven failure associated features, and ocean bottom-current activities. Besides, marine biologists were able to investigate deep-ocean benthic habitats. Similarly, in Turner et al. (2018), the distribution of the benthic communities of the Ningaloo Marine Park, Australia, was analyzed using geomorphological measurements provided by an MBES device, environmental data (such as the water temperature, salinity, to mention a few), and optical images. The exploited data set was acquired in several surveys conducted by different AUVs. In Schrottke et al. (2006), an AUV able to acquire high-resolution photographic, bathymetric, and subbottom data was used to perform a seismo-acoustic characterization. An optical delineation campaign of near-shore benthic habitat was reported in Moline et al. (2007). The exploited AUV was equipped with multi-spectral radiometers and optical cameras; the results demonstrated AUVs' ability to map littoral habitats at high resolution and proved their fundamental role in collecting high-quality data for science users. Marine vehicles were also employed for water-quality monitoring, and observation of fish behavior in net cage fish farming (Karimanzira et al., 2014), where collecting data over large areas is of utmost importance.

Finally, AUVs found extensive use in seabed inspections. In these tasks, the vehicle is used to collect optical as well as acoustic images, using cameras and imaging SONARs. Then, the data could be used for underwater surveillance purposes (Terracciano et al., 2020), where image processing techniques and modern Deep Learning (DL) methodologies can accurately find targets of interest (see Jin et al., 2019; Zacchini, Franchi, et al., 2020; Zacchini, Ridolfi, Topini, et al., 2020), and for archeological investigations, where optical (Allotta, Costanzi, et al., 2016) and acoustic reconstructions (Franchi et al., 2018) emerged as an essential tool to correctly classifying historical finds.

The aforementioned case studies' analysis highlights the science users (e.g., archeologists, oceanographers, and biologists) and navy personnel necessity for robots for collecting high-quality data to analyze and study an area of interest. Science users cooperate with technicians to plan AUV surveys, often using lawnmower or zig-zag paths, to acquire well-distributed and representative data. Generally speaking, despite the different scopes and sensors used, the surveys are designed so that the more the area covered, the better the data collected. Thus, the better the area characterization.

Nowadays, AUVs passively store the data that are then analyzed offline after their recovery, meaning that exteroceptive sensor feedbacks are not used during the mission. Since environmental conditions cannot be forecasted, and the sensor characteristics affect the quantity and the quality of the collected data, it implies many mission replanning and repeated attempts, increasing the total cost of exploration and monitoring campaigns. This is especially the case of FLS- and SSS-based seabed inspections. The seafloor morphology and composition, as well as object shapes and positions, affect the performance of such acoustic devices. Consequently, designing offline AUV paths that ensure satisfying coverage of the area is challenging and requires time and experienced operators.

Coverage Path Planning (CPP) strategies represent an excellent solution. Sensor-driven algorithms can actively consider sensor feedbacks and environmental information; they can monitor the quality and quantity of acquired data and guarantee adequate coverage levels or exploration goals, avoiding repeated missions. Since the problem of computing a path that optimally covers an area of interest with a sensor is common to many robotic domains, several CPP methodologies for Unmanned Ground Vehicles (UGVs), Micro Aerial Vehicles (MAVs), and AUVs have been proposed in the last years. Generally speaking, the authors developed solutions to enable the robot to calculate the shortest route online through unknown areas to create occupancy maps and acquire the necessary data, requiring various sensor sets.

This study describes a coverage framework composed of a planning and a mapping module, tailored for AUVs to accomplish FLS-based seabed inspections, but that can be extended to any exteroceptive sensor. A receding-horizon sensor-driven coverage methodology based on random trees, which enables an AUV to automatically acquire well-distributed and representative data over an area of interest, is proposed and used in the planning module. It uses a three-dimensional (3D) probabilistic occupancy mapping system for

FLS reconstructions to compute the AUV viewpoints. This latter module uses FLS imagery and employs a machine learning segmentation technique to create and update the environment's occupancy map during the vehicle mission. It allows the planning module to correctly select the Next-Best Viewpoint (NBV) by evaluating tree nodes' visibility according to the map. Therefore, the AUV actively considers the sensor feedbacks during the mission and can guarantee adequate coverage of the area of interest. The here proposed framework was validated and tested on FeelHippo AUV (Allotta et al., 2017), a compact AUV developed by the Department of Industrial Engineering of the University of Florence (UNIFI DIEF). First, it was validated through an extensive set of realistic experiments made by means of the Unmanned Underwater Vehicle Simulator (UUV Simulator; Manhães et al., 2016) and real data recorded during sea trials performed with FeelHippo AUV. Then, an experimental campaign to demonstrate the effectiveness of both the mapping and planning methodologies was conducted; the results are reported and discussed.

This article remainder is organized as follows: Section 2 details paper's contribution and reviews related state-of-the-art works, whereas Section 3 describes the considered problem and presents the preliminaries of path planning and 3D mapping. Section 4 is dedicated to the description of the proposed paradigm. In particular, it reports the developed framework and describes in detail the 3D FLS-based probabilistic occupancy mapping system and the coverage methodology. In addition, Section 4 provides an analysis of the coverage solution with a theoretical investigation concerning the performance of different formulations. In Sections 5 and 6 the validation and the experimental results are reported and analyzed. Finally, Section 7 summarizes the presented research and discusses future works.

2 | BACKGROUND AND PAPER CONTRIBUTION

This section highlights the main characteristics of the here proposed strategy and reports related works that inspired this study. First of all, the contributions of this paper are described, then state-of-the-art and innovative solutions for coverage and exploration tasks are presented. Lastly, previous mapping-related works are reviewed.

2.1 | Contribution

This paper investigates the development of a sensor-driven coverage framework that endows an AUV with the ability to autonomously conducting an inspection survey and ensures adequate coverage of the target area. In the underwater domain, state-of-the-art inspection missions are represented by preplanned surveys, such as lawnmower and zig-zag paths, where the AUVs passively store the collected data. Such paths can be optimized by considering the utilized sensor characteristics, but environmental conditions cannot be forecasted,

and thus, they do not guarantee the acquisition of data over the entire area of interest and could lead to repeated attempts. In the last years, some solutions to overcome these limitations have been proposed. However, as reported in Section 2.2, such CPP solutions were developed for Mine Counter Measure (MCM) applications and only considered as feedback the presence or absence of an object. Solutions for inspections of underwater structures or exploration of unknown areas could seem reasonable. Still, they either rely on a prior map or end up being a greedy strategy when it comes to CPP applications. As the aerial domain is concerned, some remarkable solutions, which could inspire an AUV tailored CPP solution, have recently been presented, but to the best of authors' knowledge, their exploitation has not been investigated by the marine community yet.

Therefore, this study paper aims at investigating, for the first time to the best of the authors' knowledge, the use of the recent advancements in the aerial domain for developing an underwater framework that can guide an AUV toward autonomous inspection surveys. The authors have sought a solution that overcomes the drawbacks of the previously mentioned approaches; that is, it does not require a prior map; it uses the expected benefit of more actions than just one, that is, does not turn into a greedy approach that leads to longer paths, and can replan online the mission by considering as feedbacks the covered area and not only the presence or absence of objects.

The AUV tailored FLS-based inspection framework presented here, suitable for any acoustic or optical sensor, which extends and fuses the short works presented in Franchi, Bucci et al. (2020) and Zacchini, Ridolfi, and Allotta (2020), was developed for ensuring that the entire seabed of the area of interest is enlightened by an FLS, which is particularly useful for objects of potential interest searching surveys (Terracciano et al., 2020; Zacchini, Franchi, et al., 2020), acoustic mosaicing (Franchi et al., 2018), and so on. In detail, a probabilistic 3D occupancy mapping methodology, based on the research work presented in Franchi, Bucci et al. (2020), was integrated with the here presented coverage planning framework, which deepens the solution described in Zacchini, Ridolfi, and Allotta (2020). The overall framework and the results reported in this paper are novel and were not presented previously. First, the innovative 3D probabilistic occupancy mapping system for FLS reconstructions is described. It uses machine learning segmentation techniques on acoustic images to generate a 3D point cloud of the seafloor and protruding visible objects, overcoming the information loss that occurs during the 3D to 2D image projection. It is worth highlighting that this mapping module was developed to provide feedback to the planning module on the area covered by the utilized imaging SONAR, that is, the enlightened seabed, and not for creating an accurate reconstruction.

The CPP methodology presented here is based on a two-level planning paradigm that allows using different planning policies and cost functions for each level. A CPP algorithm was designed for the high-level planner. It grows random trees considering the vehicle kinematic using the Dubins constraints and evaluates the tree nodes according to the updated occupancy map and information metrics.

At each iteration, the best branch is selected, and only the first node becomes the NBV that is sent to the motion planner, which computes the feasible shortest path to lead the AUV to the NBV by utilizing the rapidly exploring random tree (RRT) algorithm. The process is repeated in a receding-horizon manner, similar to the control theory that helps to reduce the coverage errors. In the context of this study, a rewiring strategy for the CPP algorithm to find for each new viewpoint candidate the best parent is proposed. Besides, a comparison of volumetric information gain (IG) metrics, along with a theoretical analysis, for underwater coverage tasks, is reported.

In conclusion, the main contributions of this paper are:

- An innovative probabilistic 3D map representation for FLS-based reconstructions that uses machine learning segmentation techniques and linear interpolation over the visible object profile.
- A sensor-driven Receding-Horizon Coverage Approach (RHCA) that uses a random trees-inspired algorithm. The coverage algorithm uses the created map to evaluate the randomly generated tree node and selects the NBV. The effect of the rewiring process in tree growing is evaluated.
- A mathematical formulation of the developed coverage algorithm and a theoretical analysis of the effects of the exploited volumetric information (VI) formulation.
- A benchmark of IG metrics for AUVs 3D coverage tasks. The CPP algorithm was tested with a volume-based and an entropy-based gain metric. The comparison results are reported and discussed. As far as the authors know, this is the first study of IG metrics for coverage tasks in the underwater domain.
- Interesting results of an experimental campaign, conducted to assess the performance of the proposed RHCA in real sea trials, are reported and analyzed.

2.2 | Related works on planning and coverage

The CPP task is integral to several robotic applications and domains. CPP algorithms have to compute a feasible path for the robot using simple motion trajectories (Cao et al., 1988) that are optimal, according to specific criteria, such as the path length or the total time to complete the coverage mission. According to Choset (2001) and Galceran and Carreras (2013), CPP algorithms are classified as offline, which requires full prior knowledge of the environment and relies on stationary information, and online, as they consider the sensor feedback. Offline algorithms are built on assumptions that might be unrealistic in many scenarios, as the underwater domain, where the conditions change continuously and rapidly, affecting both optical and acoustic payload sensors' performance. On the other hand, online strategies, also called sensor-based or sensor-driven, can deal with changing or unknown environments by considering as feedbacks the sensor measurements and reacting to the perceived environment. In this study, the problem of collecting FLS data over an area of interest, that is, FLS-based inspection, is considered, and since AUVs are commonly used in unknown areas where a prior map is not available, the focus has shifted to online algorithms.

In the context of underwater robotics, the CPP problem is a typical dual-use topic and was considered, for instance, for MCM applications and also extended to exploration tasks.

An online approach for SSS seabed coverage for MCM was proposed in Paull et al. (2012). The AUV employed a multiobjective optimization that combines information theory with the concept of branch entropy to compute the heading reference. The branch entropy was proposed to overcome the limitations of the IG, which is a useful tool for calculating the potential next moves' expected benefits. Still, it is not sufficient to achieve global goals when there is incomplete prior knowledge about the environment. In fact, it becomes a greedy-first search when applied to coverage tasks that could limit sensor-driven methods performance. The AUV performed constant altitude surveys in an equal-sized hexagon cell decomposed workspace. The MCM problem was also tackled in Williams et al. (2016), where a two-phase solution for adapting the survey to re-inspect potential targets was presented. These methods, however, are limited to MCM or object hunting applications since they consider as a measurement the belief about the presence or absence of an object at a location.

Inspections of underwater structures have carried the development of the research described in Galceran et al. (2014). The authors proposed a planning algorithm to compute the inspection path and a guidance strategy that uses the data perceived during the mission to adapt the vehicle trajectory to the terrain. For a similar application, in Palomeras et al. (2018), an algorithm that uses a prior map to calculate the minimum number of viewpoints that provide the maximum amount of information was presented. Then, a trajectory that guides the AUV through the computed viewpoints is computed by solving a Traveling Salesman Problem (TSP). However, to calculate the initial inspection mission, these strategies need a prior map, meaning that either it was available or the AUV had to perform a presurvey to gather a preliminary bathymetric map of the area.

To carry out underwater exploration in 3D unknown environments, Vidal and colleagues developed a two-layer planning system that considers optical and acoustic data to select the viewpoints (Vidal et al., 2020). The environment was represented with a cubic cell-based map, where each cell was labeled according to multisensor measurements. Acoustic data, provided by a multibeam SONAR, were used to determine whether a cell was occupied or not, while an estimation of the camera Field Of View (FOV) marked the cells as viewed. The view planner utilized the map to compute range and camera candidates deterministically. Then the viewpoints were generated along the surface normal at a distance determined by the sensor parameters (range and FOV). To select the best viewpoint, candidates were evaluated according to a metric function that used the distance between the robot and the viewpoint and the orientation difference. The selected NBV was sent to the motion planner layer, responsible for computing a safe and feasible path to lead the AUV to the viewpoint. To this end, the asymptotic optimal RRT* algorithm (Karaman & Frazzoli, 2011) was employed. Outstanding results were reached both in simulations and in real sea trials; the Girona 500 AUV, used as a testing platform, managed to explore

challenging unknown scenarios. Nevertheless, the view planner computed the NBV among the Frontier Points (FPs), that is, points in the regions between known and unknown spaces. Moreover, it requires a heuristic for deterministically selecting the viewpoint candidates. This strategy is the right approach for exploration tasks, but it limits the performance of CPP algorithms. De facto, it ends up being a greedy search strategy and leads to longer paths for adequate coverage levels in CPP applications.

In the context of 3D object reconstructions, it is possible to find several similarities with the CPP problem considered in this study work. In this context, researchers considered the problem of selecting the NBV to perform an active volumetric 3D reconstruction of an object with a camera attached to a mobile robot (Kriegel et al., 2015; Vasquez-Gomez et al., 2014). In Delmerico et al. (2018), which extends the work of Isler et al. (2016), an analysis of volumetric IG metrics is proposed. The voxels' entropy was used to consider the volumetric map uncertainty in the NBV selection criteria. In this paper, the voxels' entropy idea and the information metrics, shown in the works mentioned above, were considered. However, as for FP methods, considering only the next-best action makes those approaches greedy.

Finally, the coverage methodology proposed in this study was inspired by the strategies presented in Papachristos et al. (2017) and Bircher et al. (2018), where MAVs used novel path planning methods to explore unknown 3D spaces with a camera. Random trees were expanded in the free space. Each node of the tree represented a viewpoint that was evaluated according to the amount of unmapped space visible from the viewpoint. The best branch in the constructed tree was selected. Then, only the first viewpoint was executed (becoming the NBV), and the process was repeated in a receding-horizon manner. By considering the Branch Information Gain (BIG), these methods predicted the effects of more actions than just one and overcame the limitations of the IG method in unknown environments. Besides, random trees have the nonnegligible advantage of being able to implement nonholonomic constraints conveniently and can run onboard in real-time on small robots with limited computational capability. These methodologies were developed for the aerial domain for carrying out autonomous explorations with MAVs. To the best of the authors' knowledge, such random tree-based strategies have not been extended to the underwater domain yet. This paper investigates the use of receding-horizon sensor-driven random tree-based approaches for AUV coverage tasks. The here presented solution enables an AUV to autonomously inspect an unknown area and, by actively considering the sensor feedbacks, guarantees satisfying coverage levels. For the ease of the reader, Table 1 summarizes the solutions described in this section.

2.3 | Related works on mapping and FLS mapping

During the last decades, due to the favorable property of acoustic propagation in the underwater environment, acoustic devices have emerged as a strong alternative in underwater sensing. Indeed,

optical devices (e.g., optical cameras; Johnson-Roberson et al., 2017; Massot-Campos & Oliver-Codina, 2015) or LASER-based solution (Palomer et al., 2019), even if unquestionably worth, lay themselves open to water conditions. In fact, it is well known that turbidity, sediment, and lighting conditions pose relevant issues to such devices' operation, thus jeopardizing underwater sensing.

In the following, the main contributions related to acoustic mapping¹ will be outlined.

Concerning acoustic devices, a first classification can be made basing on the nature of the produced output (Ribas et al., 2010). In particular, *ranging* SONAR is echosounder, MBES, and pencil-beam SONAR, whereas *imaging* SONAR is FLS, Mechanically Scanned Imaging Sonar (MSIS), SSS, and Synthetic Aperture SONAR (SAS). For the sake of completeness, 3D SONAR solutions composed of a matrix array are available in the market (Davis & Lugsdin, 2005). However, they are typically tailored for large-scale vehicles.

This study is focused on imaging sensors, particularly FLSs, which can carry relevant benefits to the authors' best opinion. Indeed, they enable the coverage of a large portion of water, thus leading to significant scene acquisition and understanding. Moreover, it is the authors' conviction that the marine robotics community could obtain significant advantages with an FLS-based architecture. Most importantly, a single FLS can be used for several tasks. From sonograms acquisition and DL-based Automatic Target Recognition (ATR) applications (Valdenegro-Toro, 2016; Valdenegro-Toro, 2017; Zacchini, Franchi, et al., 2020; Zacchini, Ridolfi, Topini, et al., 2020), navigation (Franchi, Ridolfi, & Allotta, 2020; Franchi, Ridolfi, & Pagliai, 2020; Westman & Kaess, 2019b; Henson & Zakharov, 2018; Negahdaripour, 2013), 2D mosaicing (Ferreira et al., 2015; Franchi et al., 2018; Hurtós et al., 2015; Hurtós, Nagappa, et al., 2013), to mapping (Aykin & Negahdaripour, 2016a; Franchi, Bucci, et al., 2020; Guerneve et al., 2018; Kim et al., 2018; Ozog et al., 2015). Currently, different dedicated devices are employed for the above-mentioned applications. However, as far as costs and carrying capabilities are major constraints (i.e., smaller AUVs or, generally speaking, UUVs), multipurpose devices could be a promising approach. Furthermore, when FLSs are compared with MSISs, distortions related to the vehicle motion do not occur because of their high refresh rate. Similarly, compared with SSSs, combining returned acoustic echoes to produce an artifact of the insonified scene is not necessary, since FLSs can directly render a 2D image. Last, SAS-based solutions require accurate navigation, sophisticated signal processing strategies, and constrained path motions.

Undoubtly, employing FLSs as other wide-aperture imaging SONARs, poses relevant issues on recovering the 3D scene appearance from 2D images, as will be detailed in the following.

Concerning FLSs-based mapping frameworks, the differences among the approaches can sometimes be subtle but remarkable. Consequently, a detailed overview of the most promising and well-known approaches is listed in the following. In the treatment, specific

¹In this context, mapping is intended as the 3D reconstruction of underwater scenarios by means of acoustic devices.

TABLE 1 Planning and coverage state-of-the-art solutions

Category	References	Domain	Application	Approach	Remarks
Preplanned survey	Lawnmower or zig-zag paths	Underwater	Seabed inspections, MCM, data gathering	Survey path planned by a human operator	The surveys are designed so that the more the area covered, the better the data collected. The AUV passively stores the data that are then analyzed offline after the recovery. Thus, the exteroceptive sensor feedbacks are not used during the mission. They do not guarantee a certain level of coverage since the environmental conditions cannot be forecasted, and the sensor characteristics affect the quantity and the quality of the collected data. Repeated attempts are required
Online strategy	Paull et al. (2012)	Underwater	MCM	AUV heading reference computed by multiobjective optimization to perform constant altitude surveys in an equal-sized hexagon cell decomposed workspace	The branch entropy was used to overcome the limitations of the information gain, which is not sufficient to achieve global goals when there is incomplete prior knowledge about the environment. This solution can only consider an equal-sized hexagon cell decomposed workspace and cannot be used with an occupancy map
Online strategy with prior map	Galceran et al. (2014)	Underwater	Inspections of structures	Precomputed inspection path modified online by a guidance strategy according to the perceived data	The proposed algorithm requires a prior map of the area to calculate the initial inspection mission
Online strategy with prior map	Palomeras et al. (2018)	Underwater	Inspections of structures	A prior map is used to find the minimum number of viewpoints that provide the maximum amount of information, and a TSP is solved to compute a trajectory that guides the AUV through the viewpoints	This strategy needs a prior map to calculate the inspection viewpoints
Online strategy	Vidal et al. (2020)	Underwater	Exploration	Frontier-based solution that deterministically computes the NBV among the FP according to an occupancy map. Then, a motion planner based on the RRT* algorithm finds a safe and feasible path to lead the AUV to the viewpoint	A two-layer planning system that considers optical and acoustic data to select the viewpoints. The view planner computes range and camera candidates deterministically in the regions between known and unknown spaces. The environment was represented using a cubic cell-based map, where each cell was labeled according to multisensor measurements. The RRT* algorithm was used to compute the path to lead the AUV to the viewpoint. Selecting the NBV among the FP is a reasonable approach for exploration tasks but limits the performance of CPP algorithms since it evaluates only the information gain of one action, and thus, it ends up being a greedy search strategy
Online strategy	Isler et al. (2016) and Delmerico et al. (2018)	Aerial	3D object reconstructions	NBV selected among a set of candidates sampled from simple geometries circumscribed around the object. The volume in which the unknown object is contained is assumed known	The paper proposed an analysis of volumetric information gain metrics. In particular, the voxels' entropy was used to consider the volumetric map uncertainty in the NBV selection criteria, and different ways to quantify the information contained in the voxels were investigated. As for the solution presented in Vidal et al. (2020), considering only the next-best action makes this approach greedy

TABLE 1 (Continued)

Category	References	Domain	Application	Approach	Remarks
Online strategy	Papachristos et al. (2017) and Bircher et al. (2018)	Aerial	Exploration	A random tree-based approach where each node of the tree represented a viewpoint evaluated according to the amount of unmapped space visible from the viewpoint. The branch in the constructed tree that is expected to collect the highest gain is selected. Only the first viewpoint was executed, and the process was repeated in a receding-horizon manner	Feasible random trees expanded according to the vehicle motion constraints. Viewpoint candidates generated as nodes of a random tree, where the information gain was computed as the summation of the unmapped volume. By considering the branch information gain, the effect of more actions than just one is predicted, overcoming the limitations of the information gain method in unknown environments. Besides, it does not require a heuristic strategy for selecting the viewpoint candidates. Such random tree-based strategies were developed for explorations with MAVs, and their exploitation in the underwater domain has not been investigated yet

Abbreviations: 3D, three-dimensional; AUV, Autonomous Underwater Vehicle; FP, Frontier Point; MCM, Mine CounterMeasure; NBV, Next-Best Viewpoint; RRT, rapidly exploring random tree; TSP, Traveling Salesman Problem.

differences will be pointed out, and particular emphasis will be given to highlight, in the context of this study's application, pros, and cons of each one.

A first classification can be made basing on how the map is generated; in particular, *map with known poses* and *map with unknown poses* represent two distinct approaches. In the former, poses are assumed to be precisely known (or known with sufficient accuracy), whereas, in the latter, the problem of computing robot pose and map is solved together. This study can be categorized under the former class and a thoughtful illustration is detailed in Table 2. In contrast, a brief description of the others is presented at the end of the section. Moreover, a novel line of work of Sodhi et al. (2019), Ho et al. (2018), and Pairet et al. (2020) based on the OctoMap framework tries to provide a unique map representation useful both localization, under the Simultaneous Localization And Mapping (SLAM) paradigm, and planning. Nevertheless, this is not the core of this study.

Concerning map with unknown poses, which typically resorts to feature-based SLAM, references can be found in Huang and Kaess (2015), Shin et al. (2015), Mai et al. (2017), J. Li et al. (2018), Wang, Shan et al. (2019), and Westman and Kaess (2020), where tests are conducted either in controlled environments (Shin et al., 2015; Wang, Shan, et al., 2019), or offline (J. Li et al., 2018; Westman & Kaess, 2020). In Mai et al. (2017) feature points are manually selected.

3 | PRELIMINARIES AND PROBLEM FORMULATION

3.1 | FLS, mapping, and OctoMap preliminaries

A generic vector $\mathbf{p} \in \mathbb{R}^3$ and expressed in a frame $\{O^0x^0y^0z^0\}$ will be denoted with ${}^0\mathbf{p}$. A generic rotation matrix $R \in SO(3)$, with $R \in \mathbb{R}^6$, $RR^T = I_6$ (I_6 is the 6×6 identity matrix) and $\det(R) = 1$, will be indicated with three indices ${}^kR_i^j$, where ${}^kR_i^j$ is an operator that maps (rotates) unit vectors of the frame $\{O^jx^jy^jz^j\}$ in unit vectors of the frame $\{O^kx^ky^kz^k\}$, both expressed in the frame $\{O^kx^ky^kz^k\}$. The situation is depicted in compact form as

$${}^kR_i^k = ({}^kR_i^j)({}^kR_j^k), \quad (1)$$

where the columns of ${}^kR_i^k$ and ${}^kR_j^k$ are the projections of the unit vectors of the frame i in the frame k and of the frame j in the frame k , respectively. Given a generic ${}^kR_i^j$, if $k = j$, the three-indexes notation could not be employed (${}^iR_i^j = R_i^j$). In compact notation, a general pose can be represented with a transformation matrix T , a matrix member of the special Euclidean group in \mathbb{R}^3 :

$$SE(3) := \left\{ T = \begin{bmatrix} R & \mathbf{p} \\ \mathbf{0}^T & 1 \end{bmatrix} \mid R \in SO(3), \mathbf{p} \in \mathbb{R}^3 \right\}. \quad (2)$$

Two reference frames are usually employed by the marine robotics community; one (typically considered as *inertial*) is a local Earth-fixed

TABLE 2 Mapping with known poses state-of-the-art

Category	References	Approach	Remarks
Map with known poses	Cho et al. (2017) and Kim et al. (2019)	Scanning strategy to obtain 3D mapping via 3D point cloud generation	The generated output is a point cloud, which is not memory-efficient and not able to disambiguate among occupied/free or not visited areas (which represent a fundamental feature for robotic systems during coverage and exploration in an unknown environment) nor to fuse multiple observations probabilistically
	Aykin and Negahdaripour (2015, 2016a)	Space carving	The reconstruction of small 3D objects is addressed in simulation and experimentally. The proposed solution appears not suitable for planning purposes
	Guerneve et al. (2018)	Generative sensor model Space carving	Remarkable reconstruction of medium-sized objects (on the order of meters) both in simulation and real environment. However, the vehicle must be moved along the direction of uncertainty (SONAR vertical aperture). Moreover, the approach appears not to be easily scalable and unsuitable for online approaches and planning purposes
	Aykin and Negahdaripour (2013a, 2016b)	Generative sensor model	Estimation of the elevation angle of each pixel in a SONAR image to exactly reconstruct the interior points of an object. The method is constrained to the scenario of objects lying on the seafloor and the target surface. However, even if the method shows promising results for small-scale target with accurate reconstruction, to the authors' best opinion, it would put an overhead for the problem at hand (being detailed surface reconstruction not necessary)
	Westman and Kaess (2019b)	Generative sensor model	Improvement of the solution presented in Aykin and Negahdaripour (2013a, 2016b), the same drawbacks are still valid here
	Westman et al. (2020)	Non-Line-Of-Sight (NLOS)	To the authors' best knowledge, it represents the most novel line of work, and it provides impressive reconstructions. However, the involved optimization procedure puts relevant issues on online large underwater scene representation
	E. Hernández et al. (2009)	Occupancy grid mapping	The method is applied to Mechanically Scanned Imaging SONAR (MSIS) data; however, 2D reconstruction only is involved
	Wang et al. (2018) and Wang, Ji et al. (2019)	Occupancy grid mapping	A probabilistic 3D occupancy mapping framework is presented, where the OctoMap library (Hornung et al., 2013) is employed. However, the Inverse Sensor Model (ISM) is not specifically tailored for FLS (as in this study) and, moreover, the algorithm is not tested in large-scale scenarios
	J. D. Hernández et al. (2019)	Occupancy grid mapping	How to build a 3D scene from wide-aperture imaging SONAR (here an MSIS is employed) is not fully detailed
	Vidal et al. (2020)	Occupancy grid mapping	Multisensor (optoacoustic) mapping. However, concerning the acoustic part, a profiling SONAR is employed
Franchi, Bucci et al. (2020)	Occupancy grid mapping	The authors present an FLS-based probabilistic 3D occupancy mapping framework tailored explicitly to AUVs, which is the foundation of the hereby presented mapping framework. The mapping layer takes advantage of the OctoMap library (Hornung et al., 2013)	

Abbreviations: 3D, three-dimensional; FLS, Forward-Looking SONAR.

reference frame whose axes point, respectively, North, East, and Down (NED) $\{O^{\text{NED}}x^{\text{NED}}y^{\text{NED}}z^{\text{NED}}\}$, and the other, attached to the vehicle, denoted as $\{O^b x^b y^b z^b\}$ (Zacchini, Calabrò, et al., 2020). See Fossen (1994) for further information. In the following, superscript N will denote a quantity in the NED frame, whereas b will describe a quantity in the body one.

Concerning the FLS, let us consider a right-handed reference frame $\{O^{\text{FLS}}x^{\text{FLS}}y^{\text{FLS}}z^{\text{FLS}}\}$ located on the FLS center whose the x -axis is

directed forward and the z -axis is pointed down. The overall situation is depicted in Figure 1.

A generic 3D point $P \in \mathbb{R}^3$ with a Cartesian representation in the FLS coordinate system ${}^{\text{FLS}}P = [X, Y, Z]^T$, possesses the following spherical coordinates $[R_{\rightarrow}, \alpha, \beta]^T$, where R_{\rightarrow} is the FLS delivering range, α is the azimuth angle, and β is the elevation angle. The following relations hold:

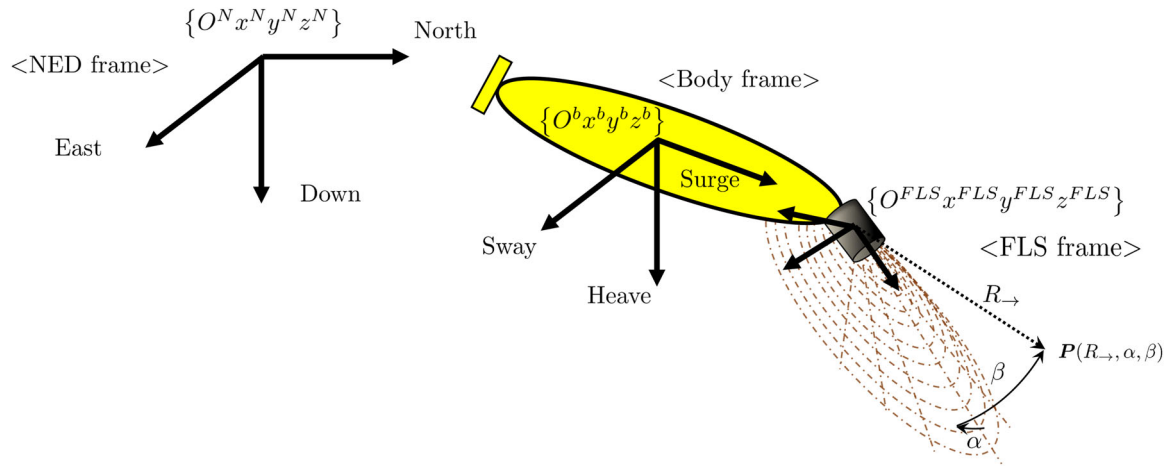


FIGURE 1 NED frame, body frame, and FLS frame representation. FLS, Forward-Looking SONAR; NED, North, East, and Down [Color figure can be viewed at wileyonlinelibrary.com]

$$\begin{aligned} \text{FLS}\mathbf{p} &= \begin{bmatrix} X \\ Y \\ Z \end{bmatrix} = R_{\rightarrow} \begin{bmatrix} \cos \beta \cos \alpha \\ \cos \beta \sin \alpha \\ -\sin \beta \end{bmatrix}, \\ \begin{bmatrix} R_{\rightarrow} \\ \alpha \\ \beta \end{bmatrix} &= \begin{bmatrix} \sqrt{X^2 + Y^2 + Z^2} \\ \tan^{-1}(Y/X) \\ \tan^{-1}(-Z/\sqrt{X^2 + Y^2}) \end{bmatrix}. \end{aligned} \quad (3)$$

FLSs are active devices, that is, they propagate sound pressure waves that are reflected by the insonified targets and recorded by the device. In particular, the transmitted pings are composed of beams that span along the FLS FOV, see angle α , with fixed elevation angle aperture, bounded by $[\beta_{\min}; \beta_{\max}]$ (the overall width is usually 7° – 20°). For each beam of the FLS, at every range interval, the measured average power, as a function of R_{\rightarrow} and α produces the intensity value of the correspondent pixel in the final FLS image, natively in the polar domain. Because of the image generation process, the originated FLS image at a particular range and beam value cannot keep track of the origin of the reflected echo along the elevation aperture (Hurtós et al., 2015). Therefore, this process poses ambiguity when a 3D scene needs to be reconstructed from single 2D images. In other words, the 3D representation of the scene from 2D images is an ill-posed inverse problem (Aykin & Negahdaripour, 2013a; Guerneve et al., 2018).

As detailed in Section 2.3, it is assumed that the robot pose is completely known (or known with sufficient accuracy) and more information concerning the navigation strategies developed by the UNIFI DIEF are detailed in authors' previous works Costanzi et al. (2016), Allotta, Caiti, Costanzi et al. (2016), and Franchi, Ridolfi, and Allotta (2020).

The employed mapping strategy resorts to the occupancy grid mapping paradigm (Burgard et al., 2005). Born as a robust representation of the surrounding environment, occupancy grid mapping (Moravec & Elfes, 1985) has encountered several marine robotics applications in the context of collision checking and obstacle/collision avoidance (Youakim et al., 2020), mapping (Franchi, Bucci, et al., 2020; Teixeira et al., 2016), planning

(J. D. Hernández et al., 2019; Vidal et al., 2020), and navigation with planning (Ho et al., 2018; Pairet et al., 2020; Sodhi et al., 2019).

Given the robot pose $x(\cdot)$, and the set of measurement $z(\cdot)$, up to the time t as $z_{1:t}$, occupancy grid tries to infer the map m from such observations. Here, the notation $(\cdot)_{1:t}$ indicates the set of data from time 1 to time t , where $t \geq 1$. In the following, for the sake of brevity, the dependence on the poses will be omitted. The classic occupancy grid theory, as exploited in the hereby presented work, employs the following assumptions:

- The grid cells m_i that partitions the 2D or 3D domain, such as $m = \sum_i m_i$, are considered as independent. As a consequence, the problem of estimating m is divided into independent subproblems. Intentionally, to make the problem tractable, dependencies among neighboring cells are explicitly not considered.
- The Markovian assumption $p(z_t | m_i, z_{1:t-1}) = p(z_t | m_i)$ is employed, where $p(\cdot | \cdot)$ represents the conditional probability. Arguably, this represents the most significant assumption that can lead to incongruity in the map construction, see Burgard et al. (2005).

In the Bayesian context, the update law becomes:

$$\frac{p(m_i | z_{1:t})}{1 - p(m_i | z_{1:t})} = \underbrace{\frac{p(m_i | z_t)}{1 - p(m_i | z_t)}}_{\text{inverse sensor model}} \underbrace{\frac{p(m_i | z_{1:t-1})}{1 - p(m_i | z_{1:t-1})}}_{\text{recursive term}} \underbrace{\frac{1 - p(m_i)}{p(m_i)}}_{\text{prior}}. \quad (4)$$

As first suggested by Moravec (1989), given log-odds ratio $l(\cdot)$, where

$$l(\cdot) = \log \frac{p(\cdot)}{1 - p(\cdot)}, \quad (5)$$

an elegant and numerically efficient update formulation for the occupancy grid problem can be obtained:

$$l(m_i | z_{1:t}) = l(m_i | z_{1:t-1}) + l(m_i | z_t) - l(m_i). \quad (6)$$

The term $p(m_i|z_t)$ is called the Inverse Sensor Model (ISM) and will be detailed in Section 4.2. In this study, OctoMap (Hornung et al., 2013) has been used as a tool to develop the 3D probabilistic occupancy mapping solution. OctoMap is a well-known and efficient open-source C++ library, ubiquitous in probabilistic robotics, for probabilistic map representation; it permits to model free $\mathcal{W}_{\text{free}}$, occupied \mathcal{W}_{obs} , and unmapped \mathcal{W}_{uk} areas, which is fundamental for planning and exploring in unknown environments. Basically, OctoMap can deal with distance-like sensor fusing measurements into a voxel representation, where the information is stored in an octree data structure. The main part of the octree is the node, which represents the space contained within a cubic volume, usually known as a voxel. Recursively, the volume is divided into eight (equally dimensioned) parts, and the procedure stops whenever a minimum size is reached. More information can be found in Hornung et al. (2013) and the references therein.

In addition to the solution presented in Equation (6), OctoMap, in its standard version, employs the noninformative prior assumption $p(m_i) = 0.5$, which is reasonable when mapping in completely unknown environments. Moreover, the clamping update policy (Yguel et al., 2008) is used, leading to

$$l(m_i|z_{1:t}) = \max(\min(l(m_i|z_{1:t-1}) + l(m_i|z_t), l_{\max}), l_{\min}), \quad (7)$$

where $l_{\min} \in \mathbb{R}^+$ and $l_{\max} \in \mathbb{R}^-$ are the lower and upper bound on the log-odds value, respectively.

3.2 | Motion planning formulation

The motion planning problem is defined as the problem of computing safe and feasible paths that the vehicle can track according to its kinematic (or dynamic) constraints. Mathematically, given an initial configuration ξ_{init} , that is, the vehicle pose, a target configuration ξ_{goal} that defines the goal region $\mathcal{W}_{\text{goal}}$, that is, a ball centered in ξ_{goal} with a predefined radius; defined the workspace \mathcal{W} , the obstacle region \mathcal{W}_{obs} , and denote the obstacle-free space as $\mathcal{W}_{\text{free}} = \mathcal{W} \setminus \mathcal{W}_{\text{obs}}$, a feasible path problem, denoted as $(\mathcal{W}_{\text{free}}, \xi_{\text{init}}, \xi_{\text{goal}})$, is defined as the task of finding a path $\sigma : [0, 1] \rightarrow \mathcal{W}_{\text{free}}$ such that $\sigma(0) = \xi_{\text{init}}$ and $\sigma(1) \in \mathcal{W}_{\text{goal}}$. The computed path σ belongs to the obstacle-free space $\mathcal{W}_{\text{free}}$ and has to be feasible, which means it must be compliant with the vehicle kinematic (or dynamic) constraints. Moreover, given the set of all paths Σ and a cost function $c : \Sigma \rightarrow \mathbb{R} \geq 0$, the optimality problem of path planning asks for finding a feasible path σ^* such that $c(\sigma^*) = \min(c(\sigma) : \sigma \text{ is feasible})$ (Karaman & Frazzoli, 2011).

Motion planning algorithms tackle this problem and find a path that satisfies the described requirements. In the context of this study work, a motion planner is used to compute the shortest path that leads the vehicle to the goal configuration; thus, it utilizes the path length as a cost function. However, it is worth noting that the multilevel planning paradigm here considered allows using any admissible cost function.

The here proposed framework was designed to run onboard on compact AUVs. The asymptotic optimal RRT* (Karaman & Frazzoli, 2011) has been proven to efficiently explore the workspace while taking the motion constraints into account. It was tested in the underwater domain for AUV onboard solutions (J. D. Hernández et al., 2019), showing satisfying results. Therefore, the RRT* algorithm with the Dubins kinematic constraints was selected as the motion planner.

3.3 | Coverage planning preliminaries and IG metrics

Although several strategies for motion planning tasks have been proposed, and sampling-based algorithms have become state-of-the-art for unknown environments, the coverage problem is still an open point in the academic and industry market. In a two-level planning paradigm, the high-level planner (also called view planner) tackles this problem. This study focused on developing a sensor-driven coverage solution that enables the robot to carry out FLS seabed inspections of an unknown area. Such surveys are typically conducted with the AUV navigating through preplanned waypoints, flying at a constant depth or at a constant altitude from the seafloor. To overcome the limitations of preplanned paths and make the AUV aware of the gathered data, the high-level planner has to compute iteratively online the next waypoint to map the unknown area. In this study, the AUV is supposed to perform a constant altitude mission; thus, the coverage algorithm was designed to compute the next waypoint constituted of a 2D position (x^N, y^N) in the NED frame and orientation (ψ) , which represents the vehicle heading angle. From these considerations, a robot viewpoint (or configuration) is defined as $\xi \in \Xi$, with $\xi = (x^N, y^N, \psi)$, and the considered problem is the following: computing online the best path according to a cost function, that let the AUV map the workspace \mathcal{W} , that is initially unknown $\mathcal{W}_{\text{uk}} = \mathcal{W}$, and classify it as free $\mathcal{W}_{\text{free}}$ or occupied \mathcal{W}_{obs} . The occupancy map paradigm, described in Section 3.1, is employed to determine the NBV and monitor the coverage progresses. Consequently, the coverage algorithm solves the problem of computing the waypoints that allow one to estimate $m = \sum_i m_i$.

Using the occupancy mapping strategy (Section 3.1), the visibility of a viewpoint ξ is defined as the set of visible voxels that are computed through a ray-casting process. The sensor characteristics define the set of rays \mathcal{R}_ξ for every viewpoint; each ray r ends when it reaches the maximum sensor range or the limit of the map or it hits an occupied voxel. Traversing the map, a ray visits a set of voxels \mathcal{X}_r . The obtainable IG from a viewpoint, denoted as \mathcal{G}_ξ is estimated as (Delmerico et al., 2018)

$$\mathcal{G}_\xi = \sum_{r \in \mathcal{R}_\xi} \sum_{x \in \mathcal{X}_r} l(x), \quad (8)$$

where $l(x)$ denotes the VI contained in the voxel x .

In this paper, a comparison of IG metrics for seabed inspections is reported. In particular, two VI formulations were considered:

the first one, denoted as volume-based VI in the following, considers the volume of unmapped cells, while the second one, called entropy-based VI, uses the concept of entropy to take into account the map uncertainty. Similarly to Bircher et al. (2018), when exploiting the volume-based VI, viewpoints' IG is computed by considering only the volume of unmapped cells, yielding to

$$I_v(x) = \begin{cases} \mu(x) & \text{if } x \in \mathcal{W}_{\text{uk}}, \\ 0 & \text{otherwise,} \end{cases} \quad (9)$$

where $\mu(x)$ denotes the volume of the voxel. As described in Section 3.1, OctoMap was used to develop the 3D probabilistic occupancy mapping solution, and since it employs the non-informative prior assumption, the VI can be written as

$$I_v(x) = \begin{cases} \mu(x) & \text{if } 0.5 - \delta \leq P_o(x) \leq 0.5 + \delta, \\ 0 & \text{otherwise,} \end{cases} \quad (10)$$

where $P_o(x)$ is the voxel probability of being occupied, and δ is a parameter that depends on the mapping sensor accuracy.

Moreover, the occupancy grid mapping paradigm allows considering the map uncertainty easily. Assumed $\bar{P}_o(x) = 1 - P_o(x)$, an entropy-based VI formulation can be defined:

$$I_e(x) = -P_o(x) \ln(P_o(x)) - \bar{P}_o(x) \ln(\bar{P}_o(x)). \quad (11)$$

Utilizing this VI formulation, the highest uncertainty matches unknown voxels, that have the occupancy probability of $P_o(x) = 0.5$.

4 | COVERAGE FRAMEWORK FOR SEABED INSPECTIONS

The developed RHCA framework for seabed inspections is described in this section. First, the framework structure and implementation details are reported. Then, the FLS mapping strategy is discussed. Finally, the developed coverage algorithm is described in detail.

4.1 | Framework structure

The here proposed coverage solution, depicted in Figure 2, is composed of four elements: the Mission Manager, the mapping module, the high-level planner, and the motion planner. These modules run onboard on the AUV and were integrated within the Robot Operating System (ROS) framework (Quigley et al., 2009). Additionally, a Graphical User Interface (GUI) that runs on a laptop computer was developed. It enables an operator or a science user to interact with the

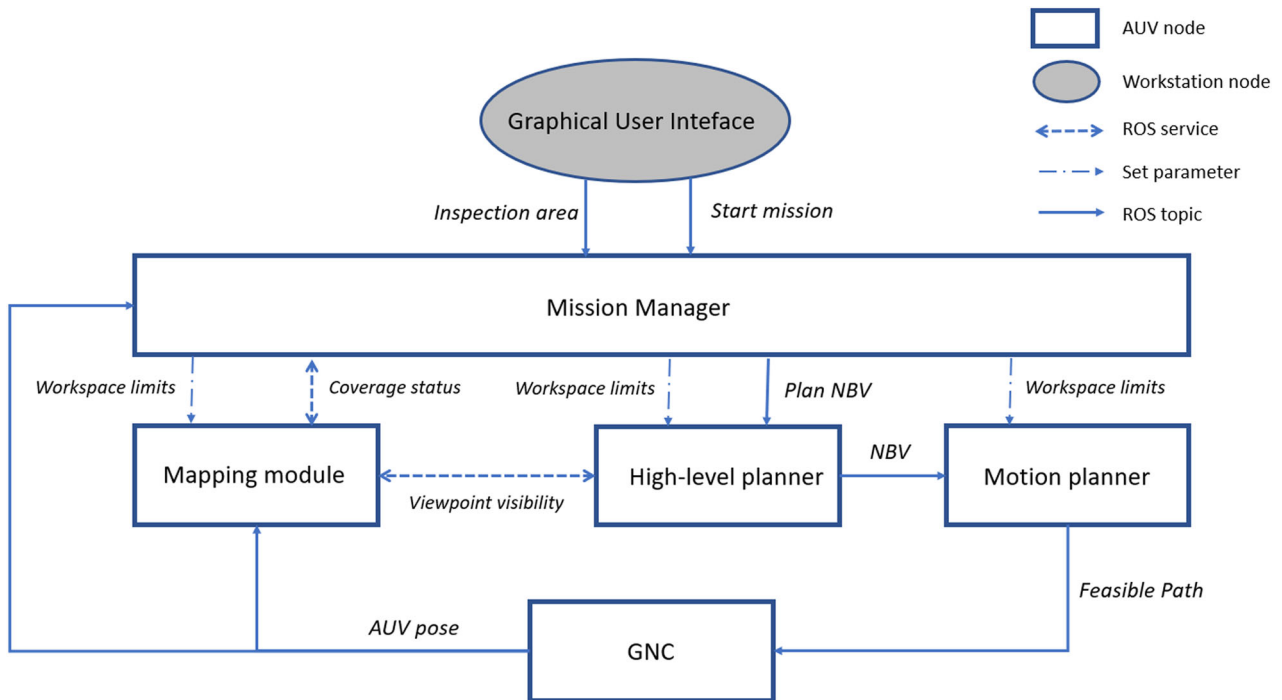


FIGURE 2 The developed inspections framework. In the context of this study, the framework was used to perform FLS seabed inspections. The operator can define the inspection area through a dedicated GUI. The Mission Manager works as an interface with the GUI, sets the workspace limits, and monitors the mission progresses. The mapping module creates and updates the map using an exteroceptive sensor. The Mission Manager triggers the high-level planner to plan the NBV to accomplish the task. Then, the selected NBV is set as the goal configuration for the motion planner, in charge of computing a feasible path for the AUV. Finally, the GNC block includes the guidance, navigation, and control strategies. AUV, Autonomous Underwater Vehicle; FLS, Forward-Looking SONAR; GUI, Graphical User Interface; NBV, Next-Best Viewpoint; ROS, Robot Operating System [Color figure can be viewed at wileyonlinelibrary.com]

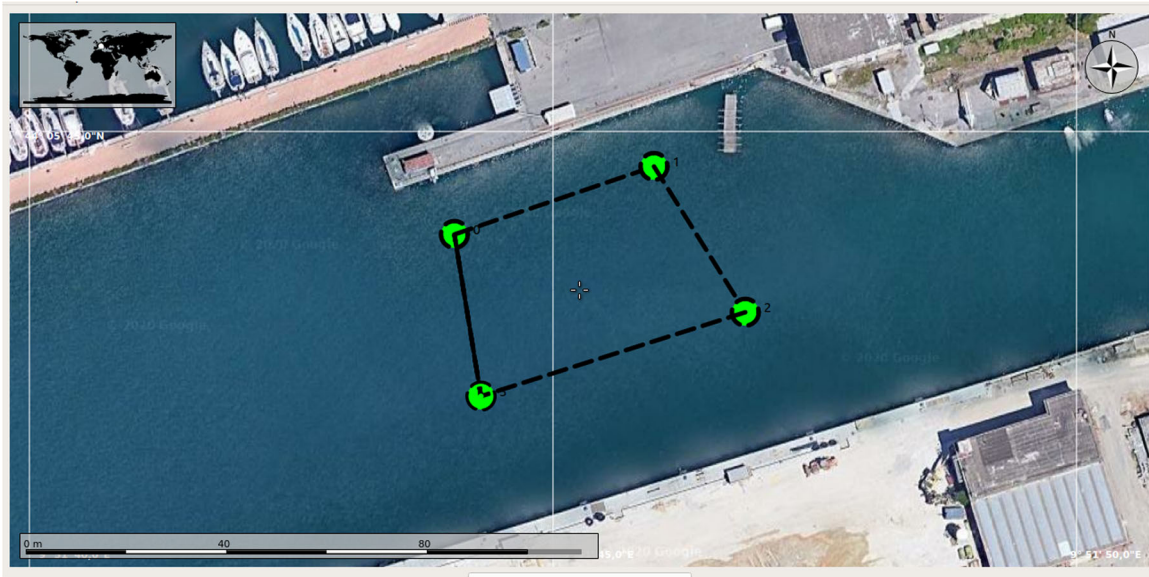


FIGURE 3 The developed Graphical User Interface (GUI) used for selecting the inspection area, limited by the four green points and the black dashed lines [Color figure can be viewed at wileyonlinelibrary.com]

AUV. As shown in Figure 3, the GUI allows one to easily define the inspection area, which is sent to the AUV through a radio or WiFi link.

The Mission Manager uses the selected inspection area to limit the workspace of other modules. It triggers the high-level planner to compute the NBV when it receives the start command from the GUI, or the vehicle has reached the previous viewpoint. It also monitors the coverage progresses.

The mapping module creates and updates an occupancy map. It takes as input the AUV estimated position and orientation and the gathered FLS images. When a new image is acquired, the module utilizes the front-end to generate a 3D point cloud and the back-end to update the occupancy map. Section 4.2 describes in detail the mapping process.

The high-level planner uses the coverage algorithm reported in Section 4.3. Starting from the AUV position, the coverage planner builds a random tree to determine viewpoint candidates. For each viewpoint candidate, its visibility is evaluated according to the updated map with a ray-casting strategy. To this end, the planner uses an ROS service to request the mapping module the viewpoint visibility, which replies with the list of visible voxels and their occupancy probability. Thus, the expected IG along the branch can be evaluated by calculating the voxels discovered along a tree branch and using one of the metrics proposed in Section 3.3. The algorithm selects the branch that is expected to collect the highest gain. The first node is extracted as the NBV, while the rest of the branch is stored, and it is used to initialize the tree when the Mission Manager requests a new NBV.

The computed NBV becomes the goal configuration of the motion planner. It is in charge of calculating the feasible best path, according to the Dubins kinematic constraints and a cost function, that leads the AUV from its position to the goal configuration. In the context of this study, the motion planner module uses the RRT* algorithm and path length as the cost function.

Finally, the GNC module includes the guidance, navigation, and control strategies that the AUV uses to estimate its position and track the planned path. This module is reported for showing how the developed framework is connected to the software architecture of an AUV, but it is not in the scope of this paper. Further information regarding the exploited GNC solutions used by FeelHippo AUV, selected as the testing platform, can be found in Allotta, Caiti, Chisci et al. (2016) and Allotta, Caiti, Costanzi, et al. (2016). For the sake of completeness, the ROS computation graph of the developed inspection framework is reported in Figure 4.

This simple structure gives the high-level planner continuous feedback of the mapped environment and enables the use of a receding-horizon approach that allows using this solution in unknown environments and helps to reduce the coverage errors. Therefore, it realizes a receding-horizon sampling-based sensor-driven coverage planning strategy.

4.2 | Mapping strategy

The mapping framework consists of two parts, see Figure 5: front-end, where 3D point cloud generation is performed (Section 4.2.1) and back-end, where occupancy mapping is achieved (Section 4.2.2).

4.2.1 | Front-end

As detailed in Section 3.1, 3D mapping from FLS images is an ill-posed inverse problem. Indeed, it requires the knowledge of the elevation angle β , which is lost during the 3D-to-2D image formation process. Although several attempts have been pursued to resolve this disambiguation, from generative models Aykin and Negahdaripour (2013a) and Westman and

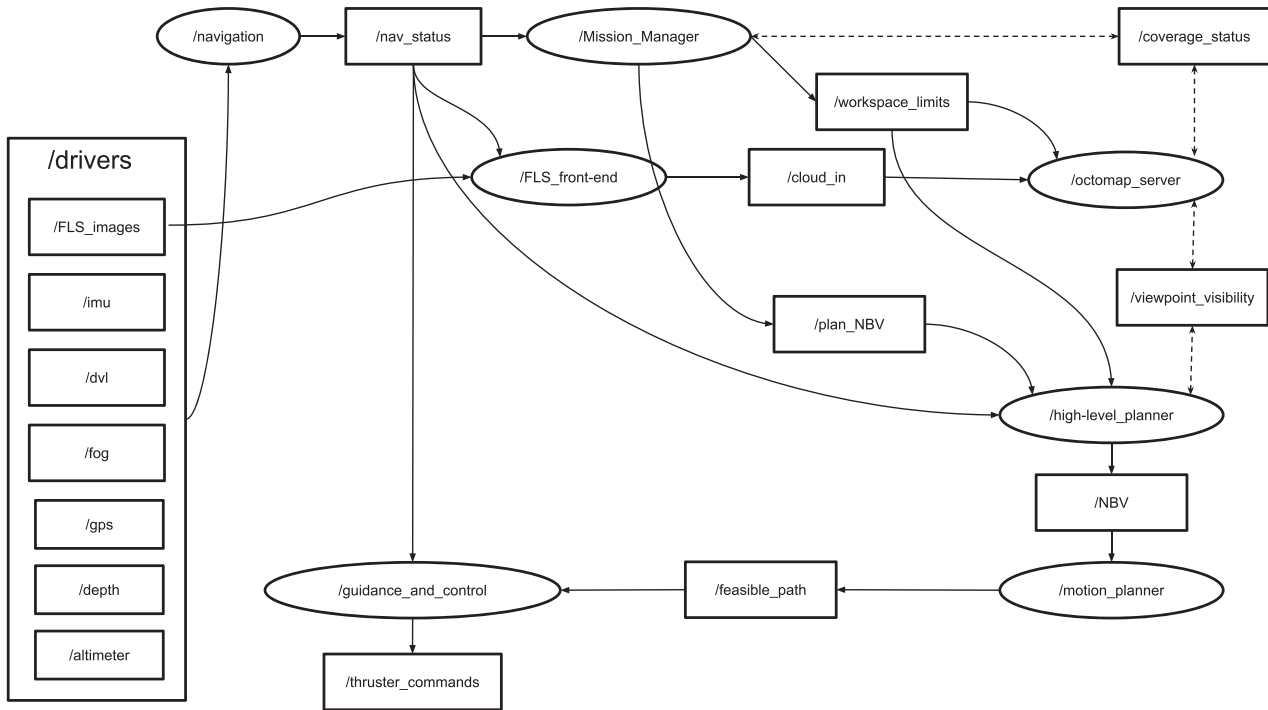


FIGURE 4 A visualization of the ROS computation graph of the developed inspection framework. Oval frames represent the ROS nodes, while squared frames depict the topics, and the continuous one-way arrows visualize the flow of information in the topics. Finally, the bidirectional dashed arrows represent the implemented ROS services. FLS, Forward-Looking SONAR; NBV, Next-Best Viewpoint; ROS, Robot Operating System

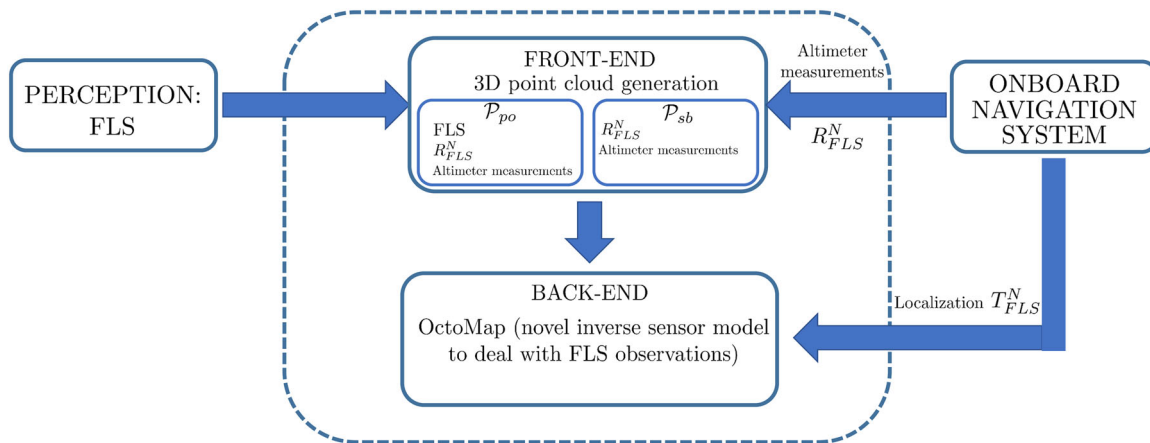


FIGURE 5 Overview of the presented mapping framework. 3D, three-dimensional; FLS, Forward-Looking SONAR [Color figure can be viewed at wileyonlinelibrary.com]

Kaess (2019b), Guerneve et al. (2018) to Non-Line-Of-Sight (NLOS) approaches (Westman et al., 2020), it is the authors' conviction that a coarser solution may fit our tasks better. In fact, the above-mentioned works provide the best reconstructions in terms of accuracy and appearance to the authors' best opinion. However, they are tailored to small reconstruction problems and are not suitable for online implementations. In the hereby presented work, the map framework must provide an adequate and time-efficient representation of the 3D environment to the planner, where the term adequate is dependent on the application at

hand. In the described application, where medium-scale environment is tested, a coarse representation of the underwater domain seems an acceptable compromise.

The hereby presented solution embraces specific ideas from Aykin and Negahdaripour (2013b) for elevation angle disambiguation and FLS image segmentation. Similarly to Aykin and Negahdaripour (2013b), the presented dense mapping framework's main assumptions are a local flat sea bottom and smooth object surfaces that change monotonically in terms of distance from the FLS.

On the one hand, the sea bottom is geometrically reconstructed based on the local altimeter measurement. On the other hand, the visible portion of protruding objects is generated according to a machine-learning segmentation technique applied to FLS images and thanks to the knowledge of the elevation angle β trend over the visible sea bottom.

The following points summarize and describe the main ideas on which the proposed strategy is based:

- The points that compose each cloud are labeled according to two sets: one set for the sea bottom \mathcal{P}_{sb} and one for the protruding objects \mathcal{P}_{po} .
- Under the local flat sea bottom assumption, the points $\in \mathcal{P}_{sb}$ are generated according to the altimeter measurements. To avoid local discontinuities, low-pass filtering on altimeter measurements is advocated.
- Inspired by the work of Aykin and Negahdaripour (2013b), it is reasonable to assume that three different levels of intensities approximately dominate each FLS image. Accordingly, intermediate brightness levels belong to flat surfaces, such as the sea bottom. In contrast, high and low levels are due to protruding 3D objects and the shadows cast by the objects (or, generally speaking, are without reflections), respectively. Consequently, the brightness profile in each FLS image is supposed to be adequately described with three classes. Trivially, each class possesses a different brightness level. To segment each FLS image, the well-known k -means clustering algorithm with seed initialization of Arthur and Vassilvitskii (2007) is employed. For further information on the k -means algorithm, please refer to Bishop (2006) and (Kanungo et al., 2002). It is worth highlighting that more advanced solutions for image segmentation, such as Convolutional Neural Networks (CNNs), could be employed. However, on the one hand, the computational burden and data collection for training, to mention a few, are significant drawbacks in applying these techniques for underwater online FLS segmentation. On the other hand, the hereby presented method based on the k -means algorithm has shown acceptable performance and can run real-time on compact AUVs without requiring dedicated hardware (see Section 5.2).

- The output of the k -means algorithm, namely, the centroid of each brightness class, is used to search the transition patterns sea bottom-to-object, object-to-shadow, and shadow-to-sea bottom. The above-mentioned transitions are used to define the object and shadow contours that, under the local flat sea bottom assumption, permit to define boundaries for the elevation angle β , namely, (β_{LE}, β_{OE}) . LE in β_{LE} stands for Leading Edge, whereas OE in β_{OE} stands for Occluding Edge; the former represents the beginning of the object profile, while the latter is the end of the object profile (see Figure 6 for more information). Within these boundaries, the elevation angle is approximated via linear interpolation, and then points $\in \mathcal{P}_{po}$ are generated, see Figure 6.
- The merging between points $\in \mathcal{P}_{sb}$ and points $\in \mathcal{P}_{po}$ is left to the back-end part (Section 4.2.2).

Given the FLS mounting angle (R_{FLS}^b) and its orientation (R_b^N), the elevation aperture of the FLS ($\beta_{max} - \beta_{min}$) and its maximum operative range, the altimeter measurements, and exploiting the local flat scene approximation, for each azimuthal scan, the FLS actual elevation angle span β'_{min} and β'_{max} can be found. It is worth noting that β'_{min} and β'_{max} can be different from β_{min} and β_{max} , and more information can be found (Aykin & Negahdaripour, 2013b). To avoid poor FLS acquisitions, the FLS maximum operative range, its mounting configuration, and its altitude need to be properly set according to the scenario at hand. Generally speaking, concerning its mounting configuration, small grazing angles (around 20°) permit to cover larger portions of the scene. In addition to this, missions at a constant altitude (around 2 m) have been conducted during the experimental trials, see Section 6 and the operative range of the FLS was set at 10 m.

Within each azimuthal scan of the FLS image, as detailed in Figure 7, the output of the k -means algorithm is used to search the transition patterns sea bottom-to-object, object-to-shadow, and shadow-to-sea bottom. Under the local flat sea bottom approximation, the elevation angle β_{OE} can be obtained from the correspondent shadow contour point. Furthermore, within the interval (β_{LE}, β_{OE}) , the trend of the elevation angle can be satisfactorily approximated via linear interpolation. It is trivial that the smoother and the monotone the surface, the more adequate the approximation. The situation is depicted in Figure 6. Generally speaking,

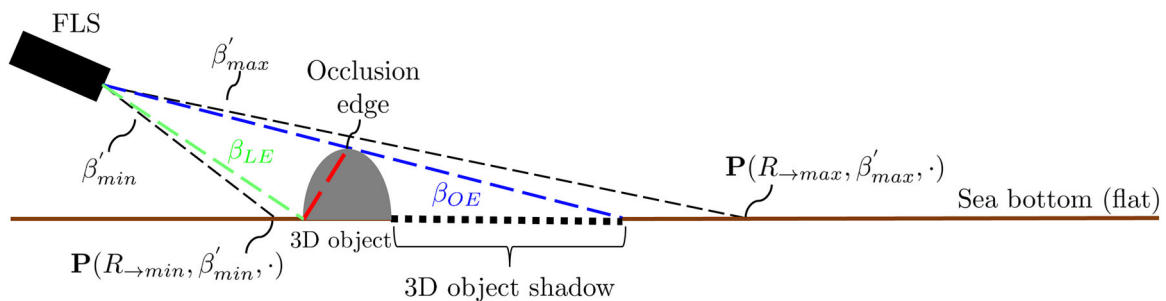


FIGURE 6 Locally flat sea bottom with a protruding object on it. Given an azimuth angle, the elevation angle at the occlusion edge can be obtained from the elevation angle of the cast shadow (see the blue line) and the end of the 3D object shadow. 3D, three-dimensional; FLS, Forward-Looking SONAR [Color figure can be viewed at wileyonlinelibrary.com]

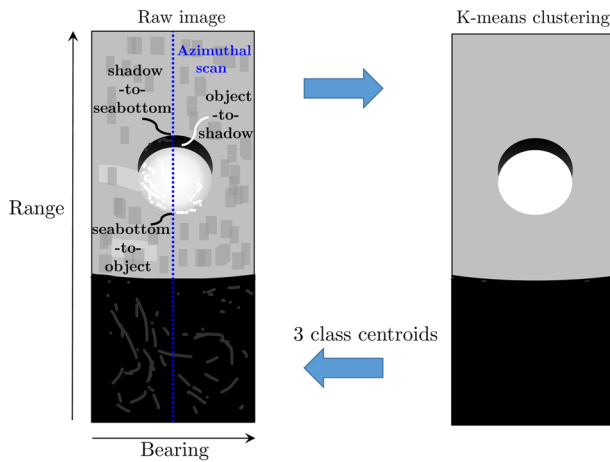


FIGURE 7 On the left, a representation of a raw FLS image. In contrast, on the right, a segmented version is depicted. The centroids of the k -means clustering algorithm are employed to search the transitions indicated on the left picture. FLS, Forward-Looking SONAR [Color figure can be viewed at wileyonlinelibrary.com]

k -means clustering offers no accuracy guarantees (Arthur & Vassilvitskii, 2006); however, its simplicity and speed have been considered a major advantage for the problem at hand. Moreover, the employment of an FLS, which is notoriously difficult due to (just to name a few) low-resolution, low Signal-to-Noise Ratio (SNR), and insonification modifications due to viewpoint changes, poses further complexity. Consequently, the k -means clustering algorithm might fail to produce results, thus impairing the following map generation. From a pragmatic and practical point of view, it is worth noting that, given the significant portions of water covered by the FLS and the typical low dynamics involved in the underwater domain, a generic object is insonified in more frames during the vehicle motion, therefore minimizing the event of not recognizing an object.

With the aim of increasing the robustness of the generated point cloud, a statistical outlier removal has been employed where, for each point, a fixed number of neighbors are analyzed, and the sample mean is computed. All the points distant more than a predetermined threshold from the mean are marked as outliers and removed from the point cloud. Moreover, to avoid the scarcity of points in the cloud (which are determined on the basis of segmentation and pattern search algorithm), up-sampling is pursued (Alexa et al., 2003). To this end, a Moving Least Squares (MLS) surface reconstruction procedure is employed (Levin, 2004) with an up-sampling method that fits the local plane (Rusu & Cousins, 2011).

The code has been implemented in C++ language by making use of the OpenCV (OpenCV, 2020) and PCL (PCL, 2020) libraries.

4.2.2 | Back-end

In its standard version, OctoMap performs ray-casting operations to update voxels, where an ISM of the form

$$l(m_i|z_t) = \begin{cases} l_{\text{occ}} & \text{if } m_i \text{ is hit by the beam,} \\ l_{\text{free}} & \text{if } m_i \text{ is traversed by the beam} \end{cases} \quad (12)$$

is employed. Here, $l_{\text{occ}} \in \mathbb{R}^+$ and $l_{\text{free}} \in \mathbb{R}^-$ are usually fixed (and selected basing on the instrument accuracy). In particular, OctoMap, born to naturally deal with range-like sensors, assigns obstacle surfaces to measurement endpoints and free space to the line of sight between the sensor origin and each endpoint, and the update law in Equation (7) is employed.

First, let us analyze the occupancy mapping related to the points \mathcal{P}_{po} .

One of the main paper contributions is focused on proposing a modified ISM to specifically account the presented front-end part of the mapping strategy (see Section 4.2.1). In particular, inspired by the work of Heng et al. (2014), this study presents an ISM obtained by discretizing a piecewise function constituted of two Gaussians centered on the measurement. To account the underlying 3D point cloud generation process, the peak amplitude is heuristically derived from metrics related to the k -means algorithm and from the brightness value of the detected object and shadow contour, therefore driving towards a non-static, self-adapting approach. A similar contribution concerning was presented in E. Hernández et al. (2009), where only the intensity of the echo was considered for 2D occupancy mapping, and a simple three-valued ISM (leveraged on echo intensities) was employed.

Mathematically, $p(m_i|z_t)$ is described as a function of the current range r and the measurement range r_z , $p(m_i|z_t) \approx p(r, r_z)$:

$$p(r, r_z) = \begin{cases} p_{\text{free}} + (a + p_{\text{occl}} - p_{\text{free}})e^{-\frac{1}{2}\left(\frac{r-r_z}{\sigma_1}\right)^2} & \text{if } 0 < r \leq r_z, \\ p_{\text{occl}} + ae^{-\frac{1}{2}\left(\frac{r-r_z}{\sigma_2}\right)^2} & \text{if } r > r_z. \end{cases} \quad (13)$$

$p(r, r_z)$ is the occupancy probability at distance r given the measurement r_z , p_{occl} is the probability for points beyond the measurement r_z (points beyond the measurement, occluded by the measurement, present $p_{\text{occl}} = 0.5$), σ_1 is the variance of the measurement (in this study it is assumed constant), and σ_2 is chosen to have an approximate symmetric distribution around r_z . In particular, a encodes the heuristics employed to weight the occupancy probability, and it is calculated as in Equation (15). In other words, the main idea is to concentrate a description of the front-end process into a . More in detail, a global descriptor,² related to the goodness of the overall segmentation process, and a local descriptor,³ which consider the goodness of the patterns bottom-to-object, object-to-shadow, and shadow-to-sea bottom are advocated.

²Global descriptor is intended a quantity that considers the whole FLS image.

³Local descriptor is intended a quantity that considers a single azimuthal scan on the FLS image.

Concerning the global descriptor, the well-known k -means clustering-related metrics sum of squared errors is used:

$$J = \sum_{n=1}^N \sum_{k=1}^K r_{nk} \|x_n - \mu_k\|^2, \quad (14)$$

where x_n is a generic element of the data set of size N , μ_k is the centroid of the cluster K , and $r_{nk} \in \{0, 1\}$ is one if data point x_n is assigned to cluster k , otherwise is zero. Such a function needs to be scaled, and thus the relative quantity J_{\min}/J is used, where J_{\min} is the minimum of J during the underwater mission. Concerning the local descriptor, without losing generality, let us consider single-channel FLS images $I: \Omega \subset \mathbb{R}^2 \mapsto \Gamma$ with $\Gamma = \{0, 1, \dots, \Gamma_M\}$, where to denote the pixel intensity at the location Z on the image I the notation $I|_Z$ is employed. For each azimuthal scan, three significant points are recognized: **Ob** is object point in the sea bottom-to-object transition, **Sh** is the shadow point in the object-to-shadow transition, and **Sb** is the sea bottom point in the shadow-to-sea bottom transition, see Figure 8. a encodes all the single local and global contribution as additive terms as follows:

$$a \propto \frac{\frac{J_{\min}}{J} + \frac{I|_{Ob}}{\Gamma_M} + \frac{\Gamma_M - I|_{Sh}}{\Gamma_M} + \frac{I|_{Sb}}{\Gamma_M}}{4}, \quad (15)$$

where α (directly proportional to) is employed to have a that gives peaks smaller than one.

Concerning the points that belong to the sea bottom, the simple ISM detailed in Equation (12) has been deemed as sufficient. However, failures in the generation of \mathcal{P}_{po} might lead to the elimination of protruding objects from the map, forcing towards a smooth and flat scenario. Indeed, protruding objects, if not detected continuously, can be deleted from ray-casting operations on \mathcal{P}_{sb} , which is indeed created from simple altimeter measurements under the local flat sea bottom hypothesis. It is worth noting that failures in the generation of \mathcal{P}_{po} can occur due to, to name a few, low-resolution, inhomogeneous insonification, and speckle noise. In conclusion, to create a unique occupancy mapping from \mathcal{P}_{sb} and \mathcal{P}_{po} , ray-casting operations on \mathcal{P}_{sb} set m_i as free space only if the corresponding voxel is not already marked occupied by protruding objects. In other words, when such “collisions” take place, the map remains static locally. The above-mentioned solutions, even if fictitious, have shown reliable reconstruction performance, maintaining the appearance of objects

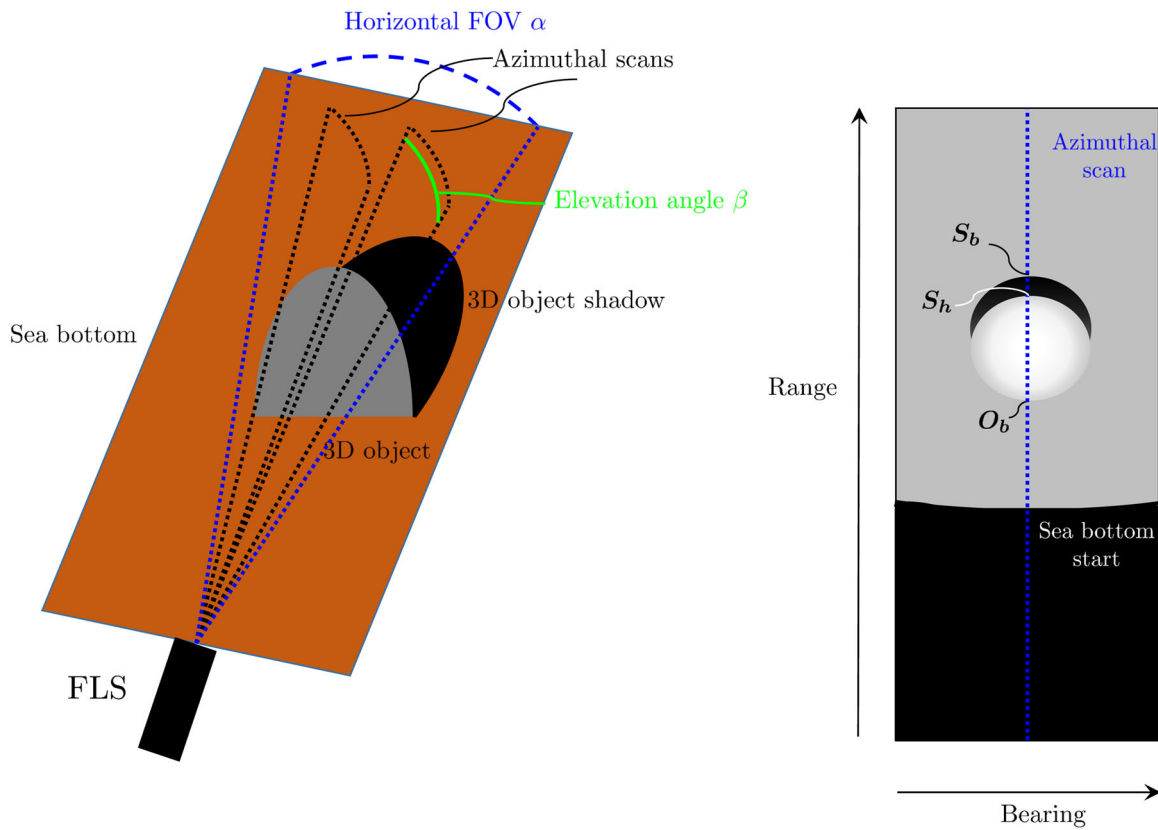


FIGURE 8 On the left, a 3D view of the sea bottom with a 3D object. The horizontal FOV of the FLS is marked in blue, whereas two azimuthal scans are depicted in a dotted black line. Last, the elevation angle is represented in green. On the right, a qualitative FLS acquisition coming from the 3D scene on the left. Given the current azimuthal scan (dotted blue line), the object point in the sea bottom-to-object transition (**Ob**), the shadow point in the object-to-shadow transition (**Sh**), and the sea bottom point in the shadow-to-sea bottom transition (**Sb**) are indicated. 3D, three-dimensional; FLS, Forward-Looking SONAR; FOV, Field Of View [Color figure can be viewed at wileyonlinelibrary.com]

that protrudes from the sea bottom and thus a realistic map for planning purposes. Moreover, the ability to dynamically react to changes and to cope with FLS noise still remains. Indeed, the occupancy map generated from FLS acquisition is free to update according to the classic update law given in Equation (7).

4.3 | Random tree-based coverage solution for high-level planning

As described in Section 4.1, the high-level planning module computes online the path to accomplish the coverage survey. In the framework proposed here, whenever the Mission Manager requests to plan the next waypoint, the high-level planner computes the NBV resorting to an RRT-inspired coverage algorithm. The developed algorithm, summarized in Algorithm 1, takes as input the AUV actual configuration. A new tree \mathcal{T} containing the AUV configuration is initialized (line 3). If the algorithm had already been activated, the remainder of the previous call solution, that is, the remainder of the best branch, is added to the tree, and its expected gain is evaluated according to the new updated map (lines 5–7). Then, until the terminal condition, which is the maximum planning time $time_{max}$ is reached, the algorithm expands the tree \mathcal{T} : it randomly samples a new configuration ξ_s in the workspace, the nearest node in the tree is retrieved ξ_n , and a new configuration ξ_{new} is computed by propagating ξ_n along the direction to ξ_s with a random step (lines 8–10). If the generated new node ξ_{new} is inside the inspection area and the motion $\xi_n \rightarrow \xi_{new}$ is valid (line 11), ξ_{new} is added to the tree \mathcal{T} (line 12). The algorithm requests to the mapping module the visibility of ξ_{new} , which responds with the observable voxels computed by using the ray-casting process (line 13). It is worth noting that the visibility of a viewpoint does not depend on the parent of the node; only its gain is affected by the choice of the parent. In fact, to correctly evaluate the expected viewpoint gain, the voxels already seen along the branch shall not be considered. This simple consideration constitutes the rewiring strategy. Once the viewpoint visibility has been computed, the algorithm looks for the best parent, that is, the parent that maximizes the gain, among the nearest nodes in the tree. Therefore, the list of the k -nearest nodes of ξ_{new} is retrieved (line 14), and for each node in the list ξ_p , if the motion $\xi_p \rightarrow \xi_{new}$ is valid (line 16), the branch gain assuming ξ_p as the parent is computed (line 17). To calculate the branch gain, the viewpoint IG of Equation (8) was extended to define the BIG $\mathcal{G}_{\mathcal{B}}$ as follows:

$$\mathcal{G}_{\mathcal{B}} = \sum_{\forall x \in \mathcal{X}_{\mathcal{B}}} I(x), \quad (16)$$

where $\mathcal{X}_{\mathcal{B}}$ denotes the observable voxels along the branch \mathcal{B} , and $I(x)$ is the voxel VI, which is calculated according to Equation (10) or Equation (11).

Then, the branch gain is computed by combining the BIG with penalizing factors. Since this study focuses on FLS seabed inspections, long and curvy paths were penalized:

$$\text{Gain}_{\mathcal{B}} = \mathcal{G}_{\mathcal{B}} e^{\lambda_{\psi}(\Delta\psi(\xi_0, \xi_k))} e^{\lambda_d(\text{distance}(\xi_0, \xi_k))}, \quad (17)$$

where $\lambda_{\psi} \in R$ penalizes curvy paths by considering the heading changes, and $\lambda_d \in R$ penalizes long paths.

Finally, the branch that is expected to collect the highest IG is selected as the solution (lines 18–21) and stored to initialize the next call (line 22). The first node becomes the NBV that is sent to the start-to-goal planner (line 23).

The presented coverage algorithm was developed using the Open Motion Planning Library (OMPL; Şucan et al., 2012), and was implemented using the C++ programming language and integrated within the ROS framework.

4.3.1 | Theoretical analysis

A theoretical analysis of the proposed receding-horizon coverage solution highlights essential properties. Generally speaking, as in Bircher et al. (2018) and Vidal et al. (2020), each time a new viewpoint is requested, the high-level planner tries to solve an optimization problem. Since the environment is unknown, the best approach is to compute the next moves according to the available data, and then, when new measurements have been acquired, repeat the process. Considering the presented tree-based solution, the receding-horizon problem can be formulated as

$$\begin{aligned} & \max_{\mathcal{B}} \mathcal{G}_{\mathcal{B}} \\ & \text{s.t.} \\ & \mathcal{B} = \{\xi_0, \xi_1, \dots, \xi_{N_p}\}, \\ & \xi_i = f(\xi_{i-1}) \\ & \xi \in \mathcal{W}, \end{aligned} \quad (18)$$

where \mathcal{B} is a branch that is composed of a sequence of random length N_p of configurations (viewpoints) $\{\xi_i\}$. The function f is the relation between two consecutive vehicle configurations ξ_i and ξ_{i-1} , that, in the context of this study, was represented by the Dubins kinematic constraints.

The problem cannot be solved using deterministic optimization algorithms. In fact, a deterministic relation between the gain function (BIG) and the workspace \mathcal{W} , where the configurations $\{\xi_i\}$ are sampled, is not available (the environment is not known a priori). De facto, the only way to know the BIG associated with a configuration is to test the configuration, that is, compute the visible voxels given the available map; thus, the gain shall be considered a “black-box” function. Stochastic optimization strategies were developed to handle such problems (Törn & Žilinskas, 1989). Random search algorithms use a probabilistic approach by repeatedly sampling the feasible region, typically according to a uniform sampling distribution. They are proven to converge probabilistically to the global optimum with probability one, but the expected number of cost function evaluations grows exponentially with the feasible space dimension (Solis & Wets, 1981). Thus, they were applied to many “black-box” global optimization problems to rapidly find a suboptimal solution.

Algorithm 1 Coverage planner algorithm

```

(1) Input: AUV configuration  $\xi_t$ 
(2) Output: Next best view configuration  $\xi_{t+1}$ 
Iteration:
(3) Initialize a new tree  $\mathcal{T}$  with  $\xi_0 = \xi_t$ 
if first call then
(4) |  $g^* \leftarrow 0$ ;
else
(5) | addBranch( $\mathcal{T}, \mathcal{B}_{t-1}$ )
(6) |  $g^* \leftarrow$  updateBranchGain( $\mathcal{B}_{t-1}$ )
(7) |  $\xi^* \leftarrow$  getPreviousSolution()
end
while  $time < time_{max}$  do
(8) |  $\xi_s \leftarrow$  sampleNewConfiguration()
(9) |  $\xi_n \leftarrow$  getNearest( $\mathcal{T}, \xi_s$ )
(10) |  $\xi_{new} \leftarrow$  randomPropagation( $\xi_s, \xi_n$ )
(11) | if (not isStateInArea( $\xi_{new}$ ) or not isMotionValid( $\xi_{new}, \xi_n$ )) then
| | continue
end
(12) | addNode( $\mathcal{T}, \xi_{new}$ )
(13) | callVisibilityService( $\xi_{new}$ )
(14) |  $\mathcal{V}_{parents} \leftarrow$  getNeighbors( $\mathcal{T}, \xi_{new}$ )
(15) | for  $\xi_p : \mathcal{V}_{parents}$  do
(16) | | if (not isMotionValid( $\xi_{new}, \xi_p$ )) then
| | | continue
| | end
(17) | |  $g \leftarrow$  computeBranchGain( $\xi_p, \xi_{new}$ )
(18) | | if isGainBetterThan( $g, g^*$ ) then
(19) | | | setParent( $\xi_{new}, \xi_p$ )
(20) | | |  $g^* \leftarrow g$ 
(21) | | |  $\xi^* \leftarrow \xi_{new}$ 
| | end
end
end
(22) Save best branch  $\mathcal{B}_t$ 
(23)  $\xi_{t+1} \leftarrow$  getNBV( $\mathcal{B}_t$ )
(24) Delete  $\mathcal{T}$ 
Return:  $\xi_{t+1}$ 

```

Exploiting random trees to solve the optimization problem in Equation (18), as in this study or in Bircher et al. (2018), correspond to use a Pure Random Search (PRS) solution (Zabinsky, 2013): RRT algorithms compute random trees by randomly sampling new configurations and use a Voronoi-biased expansion strategy to explore the workspace efficiently. Hence, the theory of the PRS algorithm can be used to analyze the coverage/exploration problem. First, as explained above, the gain function is a “black-box” whose value cannot be foretold. However, it is worth to note that it depends on two factors: the number of visible voxels and the IG formulation used. Regarding the former, the number of visible voxels along a branch \mathcal{B} depends on the configurations that constitute the branch, which are randomly sampled, and on the sensor characteristics (FOV and range). The IG depends on the occupancy probability of visible voxels and the exploited VI formulation, such as the volume and entropy-based proposed in Section 3.3. Therefore, given a branch \mathcal{B} , that is,

a sequence of configurations (viewpoints), and the sensor used to accomplish the task, the set of visible voxels is defined, and the gain function of the optimization problem depends only on the VI formulation.

Since the high-level planner has a limited computing time to solve the optimization problem, according to the PSR theory, it looks for a suboptimal solution. Defined the optimum branch \mathcal{B}^* at each call of the algorithm and its gain g^* as

$$\begin{aligned} \mathcal{B}^* &= \arg \max_{\mathcal{B}} \mathcal{G}_{\mathcal{B}} \\ \mathcal{G}^* &= \mathcal{G}_{\mathcal{B}^*}, \end{aligned} \quad (19)$$

the algorithm tries to compute a suboptimal solution with a gain $\mathcal{G}^* - \epsilon$. According to Zabinsky (2013), the probability of a PRS algorithm to generate a sample with gain better than a value $c \in R$ can be defined:

$$p(c) = v(S(c))/v(\mathcal{W}), \quad (20)$$

where $v(\cdot)$ denotes the Lebesgue measure, \mathcal{W} is the workspace (where the samples are generated), and $S(c)$ is the level set:

$$S(c) = \{\mathcal{B} = \{\xi\} : \xi \in \mathcal{W} \text{ and } \mathcal{G}_{\mathcal{B}} \geq c\}. \quad (21)$$

Therefore, at each call, there is a probability

$$p(\mathcal{G}^* - \epsilon) = v(S(\mathcal{G}^* - \epsilon))/v(\mathcal{W}) \quad (22)$$

of finding a suboptimal solution. Finally, it is possible to analyze the effect of the VI on the high-level planner. Figure 9 shows the VI formulations (Section 3.3) normalized with respect to their maximum value. As discussed above, given a set of visible voxels, the gain function of the optimization problem in Equation (18) depends only on the voxels' occupancy probability and the VI used. Thus, as shown in Figure 9, according to Equation (22), since the entropy VI formulation has a larger suboptimal level set, an algorithm using such VI formulation is more likely to find a suboptimal solution than by exploiting the volume-based.

From the presented analysis, some important considerations can be drawn. The exploited VI formulation impacts the performance of the here proposed solution. A receding-horizon strategy is used in this study; thus, the last call's best solution is kept to initialize the algorithm. However, this solution was the best according to the information available in the previous step. The VI based on the entropy enhances the algorithm probability of finding a suboptimal solution within the given computation time, meaning that the algorithm is more likely to compute a new best solution. In conclusion, the

entropy VI formulation leads to a more well-posed optimization problem and could enhance the performance of the coverage algorithm. This analysis is validated with the results presented in Sections 5 and 6, where a comparison of the two VI formulations is proposed.

5 | VALIDATION

The proposed RHCA was, first, validated with simulations and real data recorded during sea trials. FeelHippo AUV, described here below, was selected as the testing platform. The mapping strategy is validated through the use of real data gathered with FeelHippo AUV. Then, the here proposed inspection framework has been validated with an extensive comparison of realistic simulations made by means of the UUV Simulator. Since conducting experimental sea trials is time and cost expansive, this validation step made through realistic simulations, has been of utmost importance. In fact, the results reported in this section aimed to validate and tune the developed coverage framework in light of the sea trials described in Section 6. In fact, during the experimental campaign, the coverage solution was tested with the parameters found in the here reported validation process.

5.1 | FeelHippo AUV

FeelHippo AUV, depicted in Figure 10, is a compact and lightweight AUV developed by the UNIFI DIEF. The main characteristics are summarized in Table 3.

The software architecture is based on the ROS framework and runs on an Intel i-7-based LP-175-Commel motherboard (main computer). Additionally, FeelHippo AUV has three payload

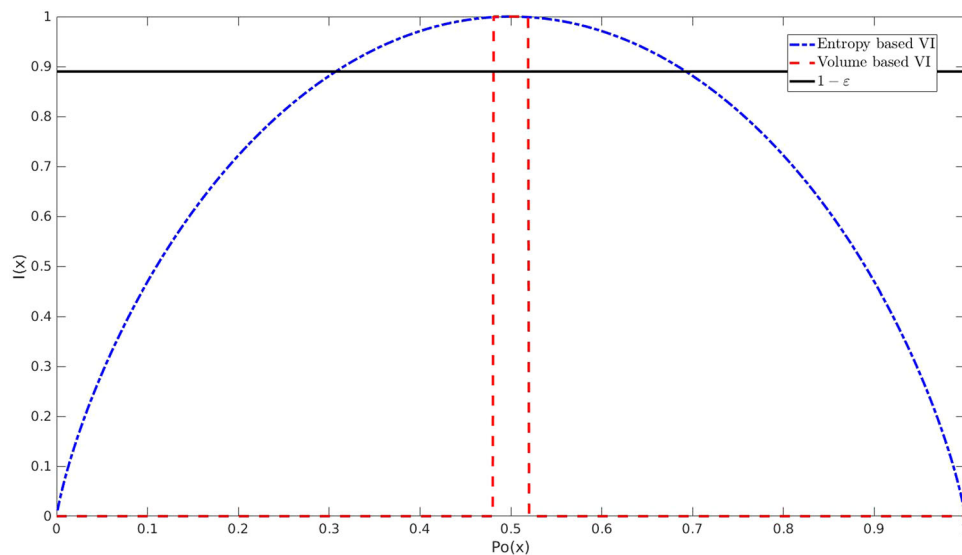


FIGURE 9 Comparison of the VI formulations normalized with respect to their maximum value. Given a suboptimal value $(1 - \epsilon)$, depicted with the continuous black line, the entropy-based VI formulation (blue dashed-dotted line) has a larger suboptimal level set than the volume-based formulation (red dashed line). VI, volumetric information [Color figure can be viewed at wileyonlinelibrary.com]

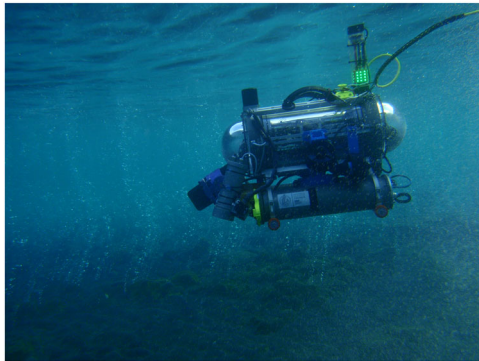


FIGURE 10 FeelHippo Autonomous Underwater Vehicle (AUV) during a sea trial [Color figure can be viewed at wileyonlinelibrary.com]

TABLE 3 FeelHippo AUV main features

Weight (kg)	35
Dimensions (mm)	600 × 640 × 500
Controlled DOFs	5
Thrusters	6
Maximum depth (m)	30
Maximum longitudinal speed (m/s)	1
Battery life (h)	3

Abbreviations: AUV, Autonomous Underwater Vehicle; DOF, degree of freedom.

computers: one NVIDIA Jetson Nano and two Intel Neural Compute Stick 2 for running onboard machine learning algorithms. Regarding the developed inspection framework, see Figure 2, it was deployed on the vehicle's main computer. The WiFi and radio links with the control station are provided by a Ubiquiti Bullet M2 WiFi access point and an 868+ RFDesign radio modem, respectively. For the sake of completeness, FeelHippo AUV can also create an acoustic link by using an EvoLogics S2CR 18/34 acoustic modem. The GNC module uses the following sensors:

- U-blox 7P precision Global Positioning System (GPS);
- Orientus Advanced Navigation Attitude Heading Reference System (AHRS);
- KVH DSP 1760 single-axis high precision Fiber Optic Gyroscope (FOG);
- Nortek DVL1000 DVL, measuring linear velocity and acting as Depth Sensor (DS);

The acoustic images used by the mapping module (Figure 2) are provided by a Teledyne BlueView M900 2D FLS with an FOV of 130°. Moreover, two bottom-looking Microsoft Lifecam Cinema cameras collect optical images.

5.2 | Mapping validation

The presented mapping strategy has been first qualitatively validated offline using data recorded during sea trials performed in 2019 at the NATO Science and Technology Organization CMRE, La Spezia (Italy), with FeelHippo AUV during the European Robotics League (ERL) Emergency 2019 competition (Ferri et al., 2017). Concerning the test, information is given in Figure 11.

The overall process is detailed in Figure 12, where the pipeline from a raw FLS image to the OctoMap representation is detailed. Last, in Figure 13, the overall results, overlaid with the mosaic presented in Figure 11 are presented.

Afterward, to provide a quantitative analysis of the mapping framework, another suitable underwater test was conducted at the Naval Support and Experimentation Centre (Centro di Supporto e Sperimentazione Navale—CSSN) basin in La Spezia, Italy with FeelHippo AUV. In particular, an object that resembles a truncated cone and whose dimensions are 0.20 m (minor radius), 0.45 m (major radius), 0.44 m (height) was placed on the sea bottom andinsonified with the Teledyne BlueView M900 2D FLS. The online generated reconstruction has been compared (in postprocessing) with the 3D model of the above-mentioned object. Turning to the quantitative analysis, the generated point cloud has been manually aligned (translation only) to the reference 3D model of the object, where the error has been evaluated by considering the median distance between the generated points and the surface of the 3D model, resulting in 0.262 m. It is worth mentioning that, on the OctoMap side, the voxel resolution was 1 cm (Figure 14).

It is worth mentioning that the presented mapping methodology is bent to the needs of the planning module and represents a trade-off between accuracy and feasibility for online operations on AUVs. In fact, although the presence of complex shapes (such as nonconvex objects) could represent a challenging scenario for the developed front-end part, the presented mapping/reconstruction module provides a meaningful and suitable representation (for autonomous planning purposes) of the surrounding environment. To the authors' opinion, given the current state-of-the-art (see Section 2.3), a more thorough and detailed reconstruction could be obtained by sacrificing online operations on small platform AUVs. Nevertheless, to the authors' knowledge, the hereby reconstruction approach is still novel; indeed, it presents for the first time an FLS-based probabilistic 3D occupancy mapping framework (integrated with an information gain-based path planning) capable of operating in large and real underwater environments without requiring particular motions for the vehicle.

5.3 | Coverage framework validation and quantitative analysis

This section presents the results of realistic simulations performed to tune and validate the coverage solution and the proposed analysis (Section 4.3). These simulations were based on the dynamic model of

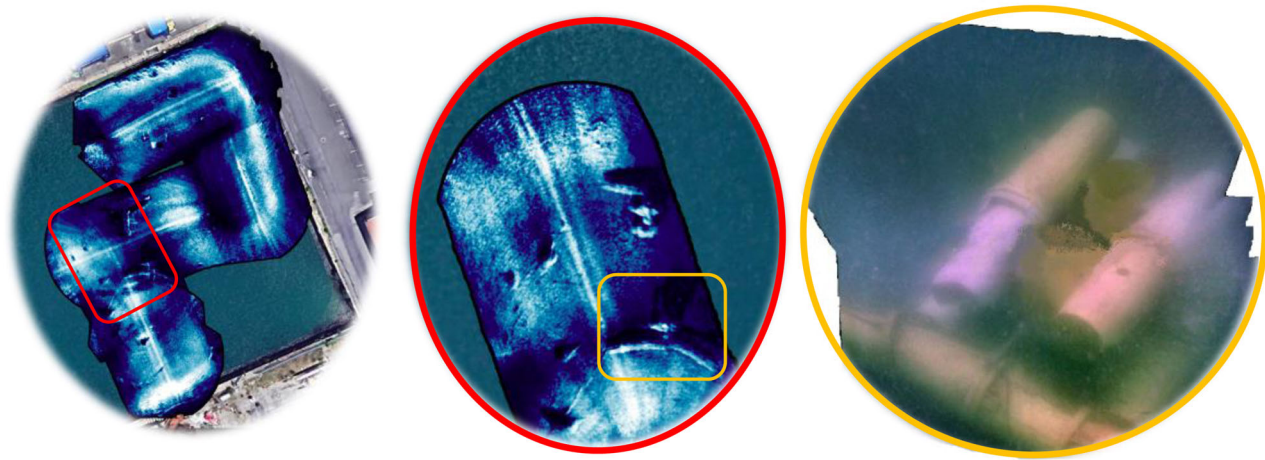


FIGURE 11 The sea bottom of the testing site. On the left, the complete acoustic reconstruction. Two underwater structures are visible within the red rectangle. In the middle, a detailed reconstruction of the area around the two underwater structures is reported. Last, on the right, five optical images are manually stitched to provide more information about the geometry of one of the two structures [Color figure can be viewed at wileyonlinelibrary.com]

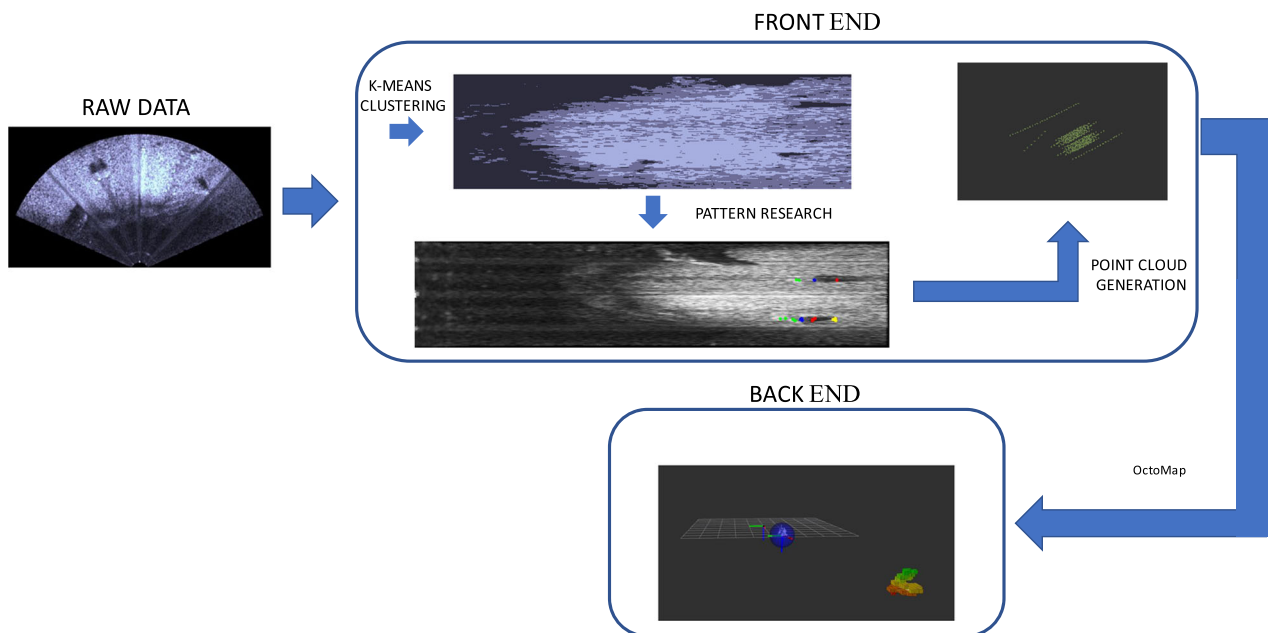


FIGURE 12 On the left, a raw Forward-Looking SONAR (FLS) image in the Cartesian domain, on the top-right its polar counterpart: two rocks are visible. Here, within the azimuthal scan, green dots represent the beginning of the object profile and blue the completion of this region. In contrast, red dots are due to the beginning of the shadow region, whereas yellow is the completion of this area. Last, on the bottom-right, the OctoMap representation of the insouffled object. It is worth noting that one of the two rocks is not generated. Indeed, the end of the shadow region is not recognized [Color figure can be viewed at wileyonlinelibrary.com]

FeelHippo AUV that was implemented in the UUV Simulator. Coverage surveys at a constant altitude of 2 m from the seabed to inspect an area of 29×27 m were simulated. To make these simulations as realistic as possible, the BlueView M900 2D FLS, which is mounted on FeelHippo AUV, was simulated through the UUV Simulator. The sensor has a horizontal FOV (hFOV) of 130° and a vertical FOV (vFOV) of 20° and the range was set to 10 m. The FLS was mounted in front of the vehicle with

a tilt angle of 30° w.r.t. the horizontal plane. The motion planner and high-level planner modules used the Dubins curves with a turning radius of 3 m to model the AUV kinematics constraints. Finally, the high-level planner maximum computing time was set to 2 s, while the RRT* employed as the motion planner had 0.5 s to find a path.

First, two lawnmower paths were designed, considering the characteristics of the sensor (FOV and range) and the target area

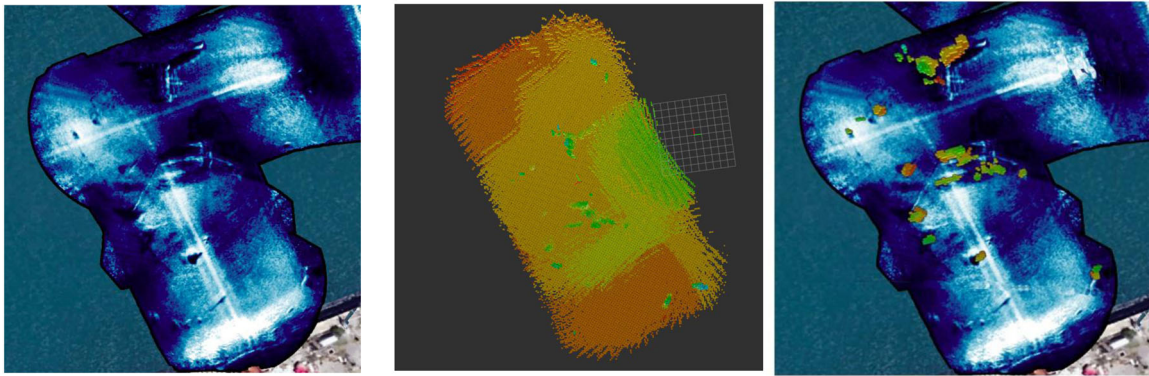


FIGURE 13 On the left, a zoom on the acoustic mosaic is presented in Figure 11. In the middle, the occupancy-grid map obtained with OctoMap. Last, on the right, the occupancy-grid map (for the sake of clarity the sea bottom is removed) is overlaid with the acoustic mosaic depicted on the left part of the image. It can be noted the good matching between the mosaic and the map [Color figure can be viewed at wileyonlinelibrary.com]

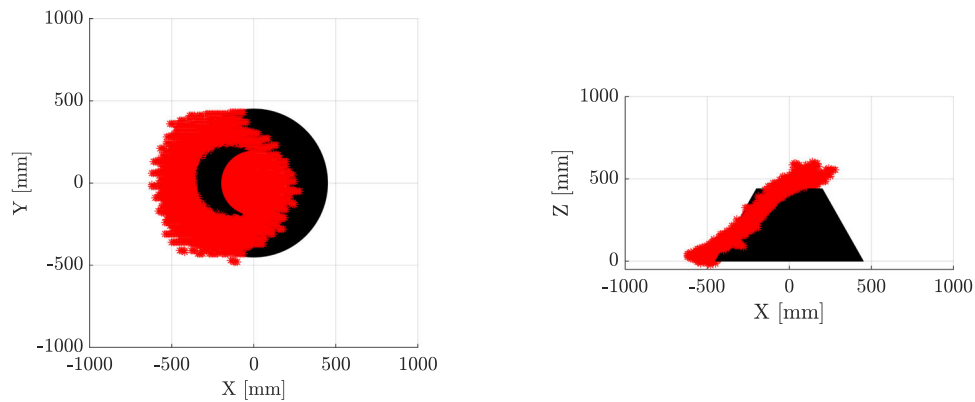


FIGURE 14 The generated point cloud in red, whereas the reference 3D model of the object is in black. On the left, the top view; in contrast, on the right, the lateral view [Color figure can be viewed at wileyonlinelibrary.com]

dimensions. As shown in Table 4, the length of the paths varies. The coverage solution was validated by performing 10 simulations with and without the rewiring strategy for both the proposed VI formulations (a total of 40 runs were performed). Since the developed coverage algorithm is based on a probabilistic approach, Table 4 reports the path length mean and standard deviation of the performed experiments. *RHCA volume* denotes the proposed RHCA with the volume-based VI, while *RHCA entropy* stands for the proposed solution using the VI formulation based on the entropy function. When the rewiring strategy is used, the algorithm tests the closest $k = 10$ neighbor nodes. The rewiring procedure is computationally expensive; this parameter was selected heuristically as a trade-off to let the algorithm evaluate a sufficient number of possible parents and generate an adequate number of samples during the given planning time.

Table 4 highlights the effectiveness of the here proposed coverage solution and points out some key aspects. The proposed RHCA solution is based on a random optimization process that varies the performance in each trial. As shown by the path length mean and standard deviation, the RHCA outperformed the lawnmower paths in

TABLE 4 Outcomes of the coverage simulations

Method	Coverage level 80%		Coverage level 90%	
	Path length mean (m)	Path length standard deviation (m)	Path length mean (m)	Path length standard deviation (m)
Lawnmower 1	102.94	-	121.31	-
Lawnmower 2	87.76	-	106.47	-
RHCA volume	98.87	9.47	126.65	16.01
RHCA entropy	89.63	9.75	123.16	13.14
RHCA volume—rewiring	95.59	7.35	124.17	13.09
RHCA entropy—rewiring	96.13	4.44	123.21	12.35

Abbreviation: RHCA, Receding-Horizon Coverage Approach.

some trials, but the planned path is longer in other experiments. However, lawnmower paths are usually developed by skilled operators, taking into account both the environmental characteristics and

the robots' payloads; the here proposed strategy could represent a solution for science users that do not require such field experts. Besides, the classic surveys may require multiple attempts. In fact, the AUV acquires data passively, without considering the quality and quantity of the gathered data. The proposed strategy instead ensures an adequate coverage level of the inspection area by actively monitoring the gathering process. Moreover, the RHCA eliminates the premission time: the AUV is deployed, and the mission can start avoiding an operator to design a suitable path that might take several minutes.

Deepening the analysis, the outcomes validate the theoretical investigation proposed in Section 4.3. The entropy-based VI formulation led to shorter paths for achieving both the 80% and the 90% of the coverage. Regarding the former goal, the RHCA entropy reached a mean path length of 89.63 m, which is close to the inspection conducted following the Lawnmower 2; while the RHCA volume, which accomplished a mean path length of 98.87 m, outperformed the survey conducted with the Lawnmower 2. The importance of the theoretical analysis of Section 4.3 emerges from comparing the RHCA results with the two VI formulations. The entropy VI formulation enhances the coverage algorithm's success probabilities of computing a solution better than the one found at the previous call. Hence, it is more likely to update the survey path than the volume-based VI. Consequently, it improves the performance of the proposed methodology.

Achieving a 90% of coverage is a more challenging task. The more the AUV covers the area, the more difficult the optimization problem of Equation (18) becomes. It means that the algorithm is less likely to change the computed old best path, leading to worse performance, that is, longer surveys. A longer planning time could lead to better performance of the RHCA, and better highlight the effect of VI formulation. Nevertheless, the planning time is a trade-off between the proposed framework's performance and the online computation constraints.

The rewiring procedure plays a key role. It remarkably reduces the variances of the computed paths. In fact, by testing different possible parents of the newly generated node, the optimization is guided toward better solutions. However, this mechanism is computationally expensive, reducing the number of generated samples within the given time. While it enhances the RHCA volume performance, it deteriorates the RHCA entropy outcomes. By generating fewer samples, it reduces the probabilities of computing new good paths, but it enables the algorithm to perform better updates, that is, the most promising branches are expanded. Although the rewiring strategy deteriorates the mean values of the RHCA entropy, it has a nonnegligible effect on its standard deviation.

6 | EXPERIMENTAL RESULTS

The proposed framework was tested in real sea trials in shallow waters, performed in October 2020 with FeelHippo AUV at CSSN basin in La Spezia, Italy. The experimental campaign aimed to

validate the coverage framework in an unknown real environment. Besides, the results validated the theoretical and quantitative analyses discussed above. An inspection area as large as the one used during the simulations (Section 5), that is, 29×27 m, was selected. FeelHippo AUV performed several surveys at a constant altitude (2 m) to inspect the seabed using the BlueView M900 2D FLS. The FLS was mounted in front of the vehicle with a tilt angle of 30° w.r.t. the horizontal plane (see Figure 15). The SONAR range was set to 10 m. The mapping module aimed to create an occupancy grid map of the covered area that is used as an active feedback for the high-level planning module. Thus, since the goal was not to create a detailed reconstruction of the environment, the map resolution was set to 0.5m. Both the motion planner and high-level planner modules modeled again the AUV kinematics constraints with Dubins curves with a turning radius of 3 m. The high-level planner had 2 s to compute the NBV. The motion planner calculated the path to lead the AUV to the NBV in 0.5 s using the RRT* algorithm.

First of all, to have a benchmark for evaluating the proposed methodology, a lawnmower survey at a constant altitude (2 m) over the selected area of interest was performed. The executed lawnmower pattern was designed considering the SONAR characteristics and its mounting pose with respect to the AUV. By following such a path, the AUV managed to cover 80% and 90% of the target area in 62.5 and 71.7 m, respectively.

The experiments showed that the developed approach led the AUV toward the inspection surveys. Figure 16 reports a sequence of snapshots of the planning process. The high-level planner used the algorithm described in Section 4.3 to grow a random tree from the AUV initial position. The best branch (whose nodes are reported in yellow in Figure 16), that is, the branch that is expected to acquire more information, was selected, and the first node became the NBV. Then, FeelHippo AUV followed the path computed by the motion planner (depicted in green). When the NBV was reached, the high-level planner grew a new random tree that was initialized using the previous best solution. As reported in Figure 16, the RHCA solution



BlueView M900 2D FLS

FIGURE 15 FeelHippo AUV endowed with the BlueView M900 2D FLS used to conduct the inspection surveys during the experimental campaign. 2D, two-dimensional; FLS, Forward-Looking SONAR; AUV, Autonomous Underwater Vehicle [Color figure can be viewed at wileyonlinelibrary.com]

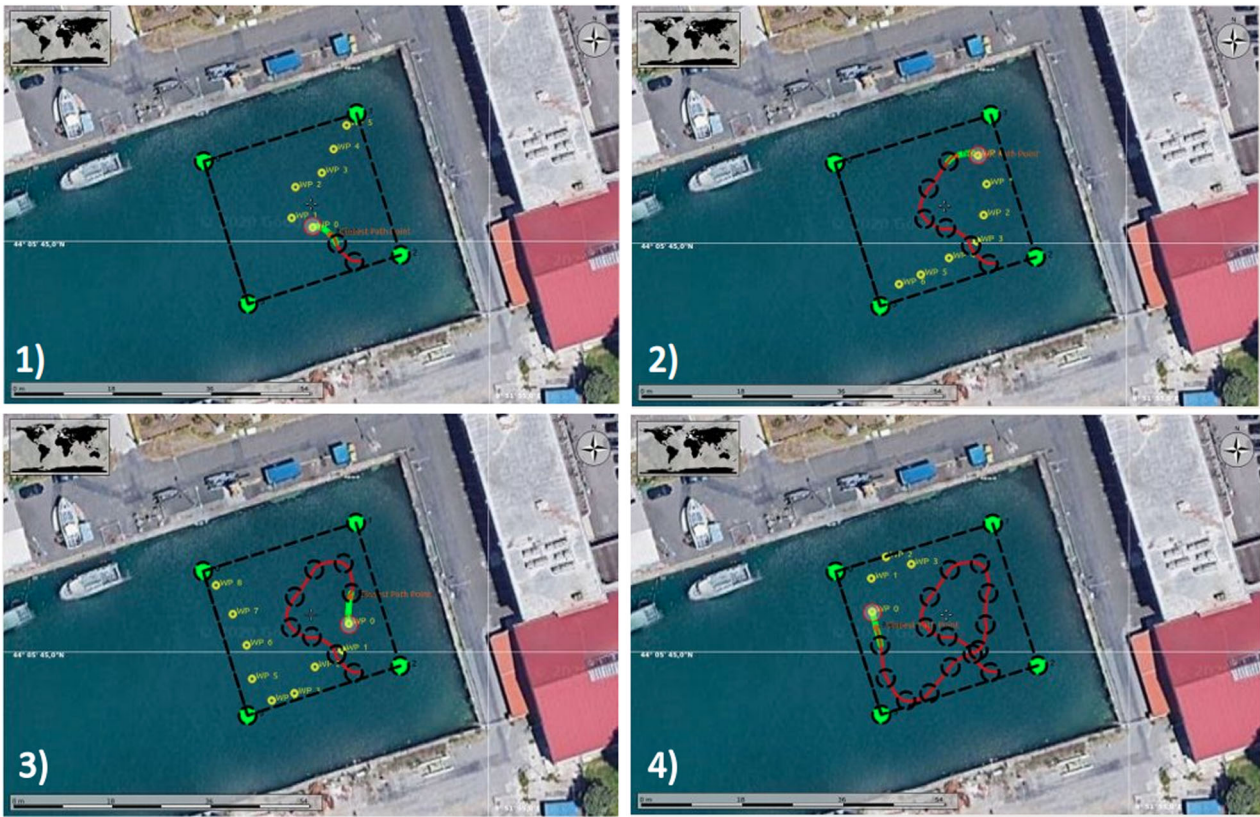


FIGURE 16 Different snapshots of one of the autonomous surveys conducted by FeelHippo AUV during the experimental campaign, La Spezia (Italy). Using the developed coverage framework, the vehicle managed to inspect the seabed of the target area, defined by the four green points and the four black dashed lines. The yellow points are the nodes of the best branch computed by the high-level planner. The path to lead the AUV to the NBV is depicted in green, while the estimated AUV tracked path is reported in red. AUV, Autonomous Underwater Vehicle; NBV, Next-Best Viewpoint [Color figure can be viewed at wileyonlinelibrary.com]

has the desired behavior: while performing the survey, the AUV can replan the mission considering the mapping module feedback.

To highlight this sought behavior, Figure 17 reports a visualization of the data collected during an inspection survey planned by the developed RHCA during the experimental campaign. While the AUV was following the inspection path, the mapping module updated the occupancy map and allowed to monitor the covered area. The map was updated using the mapping strategy described in Section 4.2 that made use of the gathered FLS images. The map's use is twofold: it is used to monitor the progress of the coverage survey and plan the NBV. In fact, as shown in Figure 17, the RHCA considers the map to move the AUV toward nonenlightened regions. The inspection path planned by the proposed high-level planner is depicted with the blue line, while the purple spheres represent the path to lead the AUV to the NBV, calculated by the motion planner, which utilizes the RRT* algorithm. In particular, it is worth noting that since the initially planned survey (Figure 17a) managed to guide the vehicle through nonenlightened regions of the area of interest, it was not modified. Each time the AUV reached a viewpoint (the blue spheres) of the inspection path, the view planning algorithm was executed, but within the given computational time, it did not find a better path (Figure 17b,c). Then, as depicted in Figure 17d, the inspection path

was updated to complete the coverage of the area. Finally, Figure 18 shows the map created by means of the developed RHCA when 90% of the inspection area was covered. Therefore, thanks to the developed solution, the vehicle inspected the seabed actively by monitoring the quantity and quality of the acquired data during the survey and using the data to replan the mission. Then, an adequate coverage level can be ensured, avoiding multiple attempts.

Turning to quantitative analysis, the RHCA was tested at field both with the volume and the entropy VI formulations. To assess the developed RHCA solution's performance in a real scenario, four trials for each VI formulation were performed: two with and two without the rewiring procedure. Table 5 reports the obtained results using the volume-based VI. The vehicle managed to inspect the area with satisfying results. In accordance with the validation experiments' outcomes, the rewiring procedure reduced the path length of the RHCA volume method. In fact, by testing possible parents of new nodes, the rewiring procedure helps the algorithm expand the branches toward the most promising directions. In Table 6 the results of the trials performed using the RHCA entropy algorithm are reported. Together with the realistic simulations, these experimental results proved the validity of the theoretical analysis of the developed coverage methodology. The entropy VI formulation leads to a more well-posed

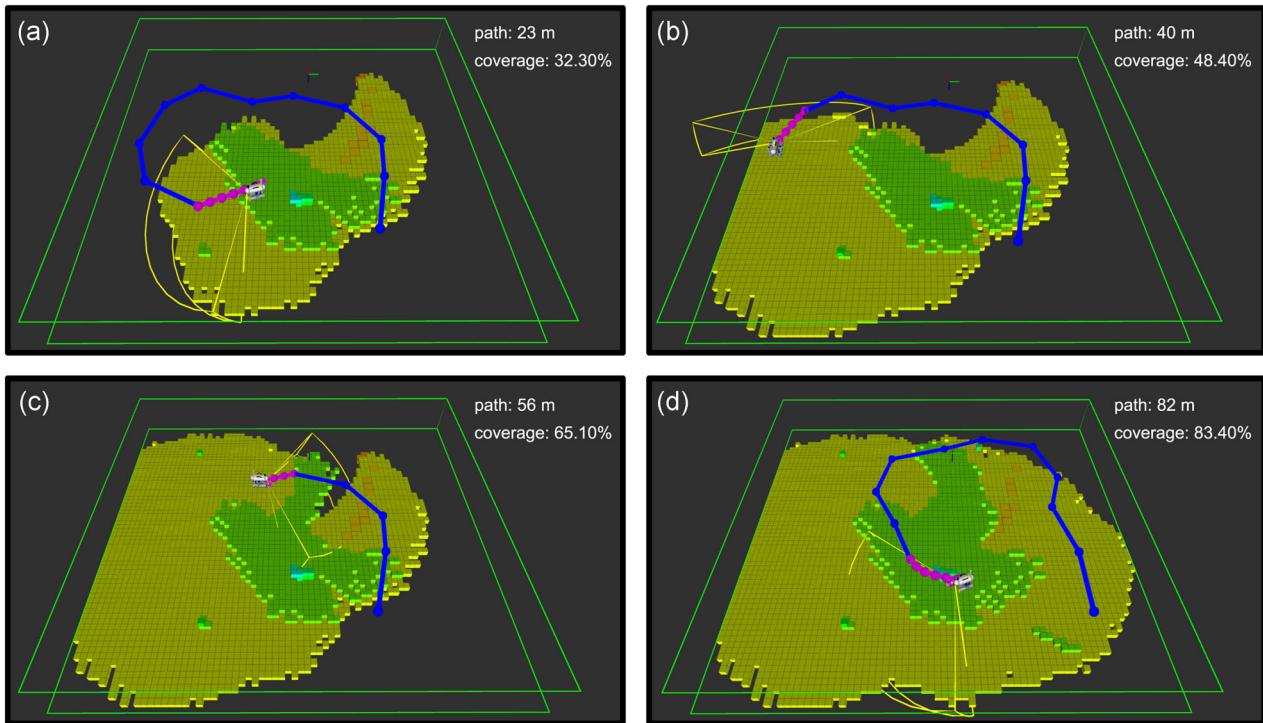
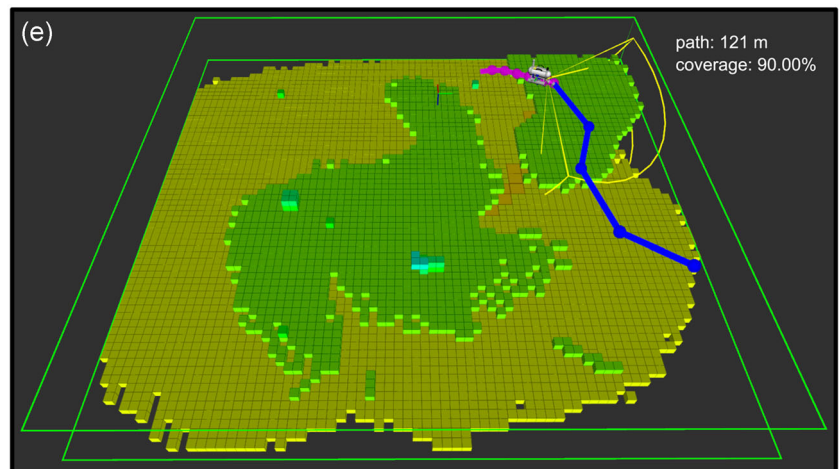


FIGURE 17 Four snapshots of an inspection survey performed by FeelHippo AUV exploiting the developed RHCA. Two green polygons delimit the inspection area at depth 0 m and the maximum depth. The mapping module uses the data gathered with the FLS, whose FOV is represented with the yellow lines, during the survey to update the map of the covered area. The inspection path generated by the high-level planner is shown with the blue line, while the purple spheres depict the path created utilizing the RRT* algorithm used as the motion planner, which the AUV tracks to reach the computed NBV. For the sake of completeness, the snapshots report, on top on the right side, the traveled distance and the reached coverage level. AUV, Autonomous Underwater Vehicle; FLS, Forward-Looking SONAR; FOV, Field Of View; RHCA, Receding-Horizon Coverage Approach; RRT, rapidly exploring random tree [Color figure can be viewed at wileyonlinelibrary.com]

FIGURE 18 The final map of the inspection area. FeelHippo AUV conducted the inspection survey autonomously by using the developed coverage solution. AUV, Autonomous Underwater Vehicle [Color figure can be viewed at wileyonlinelibrary.com]



optimization problem, and by enhancing the algorithm probability of finding a new best solution at each call, it improves the performance of the inspection framework. As shown in Section 5, the rewiring strategy deteriorates the *RCHA entropy* algorithm's performance. It is a computationally expensive process that reduces the number of generated samples. Consequently, it reduces the chances of computing new suboptimal solutions.

In conclusion, the RHCA strategy using the entropy-based VI formulation without the rewiring procedure led to better results in both simulations and real sea trials. The outcomes are in line with the theoretical discussion (Section 4.3). Besides, the experimental campaign demonstrated that the developed framework can guide the AUV toward active inspection surveys in an unknown environment and can guarantee adequate levels of coverage of the target area.

TABLE 5 RHCA volume-based VI sea trials results

Method		Coverage level 80%	Coverage level 90%
RHCA volume	Rewiring	Path length (m)	Path length (m)
Trial 1	No	88.87	118.91
Trial 2	No	91.34	114.74
Trial 3	Yes	87.82	104.53
Trial 4	Yes	83.79	110.15

Abbreviations: RHCA, Receding-Horizon Coverage Approach; VI, volumetric information.

TABLE 6 RHCA entropy-based VI sea trials results

Method		Coverage level 80%	Coverage level 90%
RHCA entropy	Rewiring	Path length (m)	Path length (m)
Trial 1	No	75.39	95.85
Trial 2	No	76.92	88.87
Trial 3	Yes	86.41	105.74
Trial 4	Yes	80.66	121.61

Abbreviations: RHCA, Receding-Horizon Coverage Approach; VI, volumetric information.

Finally, to evaluate the developed framework, the achieved results shall be compared with the ad hoc preplanned lawnmower pattern. By using both the VI formulations, the proposed methodology led to longer coverage paths than the state-of-the-art lawnmower. Nevertheless, the lawnmower path requires the perfect knowledge of the scenario and the FLS operational settings in advance, and during the mission, the AUV passively stores the acquired data. Moreover, it was calculated by a skilled operator and required a nonnegligible premission time. On the other hand, the hereby sensor-driven RHCA, being fully probabilistic, permits to obtain reasonable performance (close to the lawnmower mission) without knowing the underwater scenario in advance. In addition, it eliminates the path designing time, and by monitoring the gathered data through the created map, ensures the insonification of a required portion of the seafloor. Therefore, the developed RHCA could represent a solution for AUV end-users by simplifying the data acquisition process.

7 | CONCLUSIONS AND FUTURE WORKS

This paper presents a coverage framework to enable an AUV to perform FLS seabed inspections autonomously. The framework is composed of a mapping module, a high-level planner, and a motion planner. While the latter uses the well-known RRT* algorithm to compute feasible paths for the AUV, considering its kinematic constraints, ad hoc solutions were developed for the first two modules. The mapping module utilizes a probabilistic 3D map representation for FLS-based reconstructions.

It uses machine learning segmentation techniques and linear interpolation over the visible object profile to cope with unknown FLS elevation angles, along with an ISM to insert the FLS acquisition into a Bayesian occupancy map. A sensor-driven CPP algorithm was developed for the high-level planner. The algorithm utilizes the mapping module updated map to expand random trees and find the NBV. In fact, the visibility of each node of the tree is evaluated on the map through a ray-casting process that takes into account the FLS range and FOV. The AUV tracks the path computed by the motion planner to reach the NBV; then, the process is repeated in a receding-horizon paradigm: the previous best branch is evaluated on the updated map, and it is used to initialize the new tree. A mathematical formulation of the developed coverage algorithm and a theoretical investigation of the effects of the exploited VI formulation were provided. Besides, a comparison of two VI formulations was reported. To the authors' best knowledge, the theoretical analysis of the VI formulations is novel. This paper also presents the first investigation of information gain metrics for seabed inspections.

Real data recorded during previous sea trials verified the mapping strategy. The proposed framework was also validated with realistic simulations and then through a dedicated experimental campaign at sea. The developed solution endowed FeelHippo AUV with the ability to autonomously inspecting the seabed in a target area. By actively monitoring the data gathering process, it ensures adequate coverage levels and avoids multiple attempts. In addition, the outcomes are in accordance with the theoretical analysis; the entropy-based VI enhances the algorithm chances of computing a better solution w.r.t. the previous call and leads to better results, that is, shorter paths.

Future works will focus on improving the performance of the planning algorithm by accelerating the nodes' visibility computation. Moreover, the theoretical study suggests that reducing the space from which the samples are generated could improve the algorithm performance. Besides, a forward propagation approach to expand the tree considering the AUV dynamics, as in Y. Li et al. (2016) or Dharmadhikari et al. (2020), will be investigated. Finally, the proposed planning methodology could consider the classification of multiple targets located in the inspection area in the planning methodology.

ACKNOWLEDGMENTS

The research leading to these results has been partially supported by the European project EUMarineRobots, which received funding from the European Unions Horizon 2020 research and innovation program under grant agreement no. 731103. The authors would like to thank all the SEALab members, the joint applied research laboratory between the Naval Experimentation and Support Centre (CSSN) of the Italian Navy and the Italian Interuniversity Research Center of Integrated Systems for Marine Environment (ISME), who helped the research team during the tests at sea.

ORCID

Leonardo Zacchini  <http://orcid.org/0000-0003-3389-1631>

Matteo Franchi  <http://orcid.org/0000-0002-0786-7788>

Alessandro Ridolfi  <https://orcid.org/0000-0001-8493-7594>

REFERENCES

- Alexa, M., Behr, J., Cohen-Or, D., Fleishman, S., Levin, D., & Silva, C. T. (2003). Computing and rendering point set surfaces. *IEEE Transactions on Visualization and Computer Graphics*, 9(1), 3–15. <https://doi.org/10.1109/tvcg.2003.1175093>
- Allotta, B., Caiti, A., Chisci, L., Costanzi, R., Di Corato, F., Fantacci, C., Fenucci, D., Meli, E., & Ridolfi, A. (2016). An unscented Kalman filter based navigation algorithm for autonomous underwater vehicles. *Mechatronics*, 39, 185–195.
- Allotta, B., Caiti, A., Costanzi, R., Fanelli, F., Fenucci, D., Meli, E., & Ridolfi, A. (2016). A new AUV navigation system exploiting Unscented Kalman Filter. *Ocean Engineering*, 113, 121–132.
- Allotta, B., Conti, R., Costanzi, R., Fanelli, F., Gelli, J., Meli, E., Monni, N., Ridolfi, A., & Rindi, A. (2017). A low cost autonomous underwater vehicle for patrolling and monitoring. *Proceedings of the Institution of Mechanical Engineers, Part M: Journal of Engineering for the Maritime Environment*, 231(3), 740–749.
- Allotta, B., Costanzi, R., Ridolfi, A., Reggiannini, M., Tampucci, M., & Scaradozzi, D. (2016). Archaeology oriented optical acquisitions through MARTA AUV during ARROWS European project demonstration. In *OCEANS 2016 MTS/IEEE Monterey* (pp. 1–4).
- Arthur, D., & Vassilvitskii, S. (2006). k-means++: The advantages of careful seeding (Tech. Rep.). Stanford.
- Arthur, D., & Vassilvitskii, S. (2007). k-means++: The advantages of careful seeding. In *Discrete Algorithms Proceedings of the Eighteenth Annual ACM-SIAM Symposium* (pp. 1027–1035).
- Aykin, M. D., & Negahdaripour, S. (2013a). Forward-look 2-D SONAR image formation and 3-D reconstruction. In *2013 OCEANS-San Diego* (pp. 1–10).
- Aykin, M. D., & Negahdaripour, S. (2013b). On feature matching and image registration for two-dimensional forward-scan sonar imaging. *Journal of Field Robotics*, 30(4), 602–623. <https://doi.org/10.1002/rob.21461>
- Aykin, M. D., & Negahdaripour, S. (2015). On 3-D target reconstruction from multiple 2-D forward-scan sonar views. In *OCEANS 2015-Genova* (pp. 1–10).
- Aykin, M. D., & Negahdaripour, S. (2016a). Three-dimensional target reconstruction from multiple 2-D forward-scan sonar views by space carving. *IEEE Journal of Oceanic Engineering*, 42(3), 574–589. <https://doi.org/10.1109/joe.2016.2591738>
- Aykin, M. D., & Negahdaripour, S. (2016b). Modeling 2-D lens-based forward-scan sonar imagery for targets with diffuse reflectance. *IEEE Journal of Oceanic Engineering*, 41(3), 569–582.
- Bircher, A., Kamel, M., Alexis, K., Oleynikova, H., & Siegwart, R. (2018). Receding horizon path planning for 3D exploration and surface inspection. *Autonomous Robots*, 42(2), 291–306.
- Bishop, C. M. (2006). *Pattern recognition and machine learning*. Springer.
- Burgard, W., Fox, D., & Thrun, S. (2005). *Probabilistic robotics*. The MIT Press.
- Cao, Z. L., Huang, Y., & Hall, E. L. (1988). Region filling operations with random obstacle avoidance for mobile robots. *Journal of Robotic Systems*, 5(2), 87–102.
- Caress, D. W., Thomas, H., Kirkwood, W. J., McEwen, R., Henthorn, R., Clague, D. A., Paull, C. K., Paduan, J., Maier, K. L., & Reynolds, J. (2008). High-resolution multibeam, sidescan, and subbottom surveys using the MBARI AUV D. Allan B. In Reynolds, J., & Greene, G. (Eds.), *Marine habitat mapping technology for Alaska*. Alaska Sea Grant College Program, University of Alaska. (pp. 47–69).
- Cho, H., Kim, B., & Yu, S.-C. (2017). AUV-based underwater 3-D point cloud generation using acoustic lens-based multibeam SONAR. *IEEE Journal of Oceanic Engineering*, 43(4), 856–872.
- Choset, H. (2001). Coverage for robotics—A survey of recent results. *Annals of Mathematics and Artificial Intelligence*, 31(1–4), 113–126.
- Costanzi, R., Fanelli, F., Monni, N., Ridolfi, A., & Allotta, B. (2016). An attitude estimation algorithm for mobile robots under unknown magnetic disturbances. *IEEE/ASME Transactions on Mechatronics*, 21(4), 1900–1911.
- Davis, A., & Lugsdin, A. (2005). High speed underwater inspection for port and harbour security using Coda Echoscope 3D sonar. In *Proceedings of OCEANS 2005 MTS/IEEE* (pp. 2006–2011).
- Delmerico, J., Isler, S., Sabzevari, R., & Scaramuzza, D. (2018). A comparison of volumetric information gain metrics for active 3D object reconstruction. *Autonomous Robots*, 42(2), 197–208.
- Dharmadhikari, M., Dang, T., Solanka, L., Loje, J., Nguyen, H., Khedekar, N., & Alexis, K. (2020). Motion primitives-based path planning for fast and agile exploration using aerial robots. In *2020 IEEE International Conference on Robotics and Automation (ICRA)* (pp. 179–185).
- Escartín, J., Mevel, C., Petersen, S., Bonnemains, D., Cannat, M., Andreani, M., Augustin, N., Bezos, A., Chavagnac, V., Choi, Y., Godard, M., Haaga, K., Hamelin, C., Ildefonse, B., Jamieson, J., John, B., Leleu, T., MacLeod, C. J., Massot-Campos, M., & Garcia, R. (2017). Tectonic structure, evolution, and the nature of oceanic core complexes and their detachment fault zones (13°20'N and 13°30'N, Mid Atlantic Ridge). *Geochemistry, Geophysics, Geosystems*, 18(4), 1451–1482.
- Ferreira, F., Djapic, V., Micheli, M., & Caccia, M. (2015). Forward looking SONAR mosaicing for mine countermeasures. *Annual Reviews in Control*, 40, 212–226.
- Ferri, G., Ferreira, F., & Djapic, V. (2017). Multi-domain robotics competitions: The CMRE experience from SAUC-E to the European Robotics League Emergency Robots. In *OCEANS 2017-Aberdeen* (pp. 1–7).
- Fossen, T. I. (1994). *Guidance and control of ocean vehicles*. John Wiley & Sons.
- Franchi, M., Bucci, A., Zacchini, L., Topini, E., Ridolfi, A., & Allotta, B. (2020). A probabilistic 3D map representation for forward-looking SONAR reconstructions. In *2020 IEEE/OES Autonomous Underwater Vehicle Workshop (AUV)* (pp. 1–8).
- Franchi, M., Ridolfi, A., & Allotta, B. (2021). Underwater navigation with 2D forward looking SONAR: An adaptive unscented Kalman filter-based strategy for AUVs. *Journal of Field Robotics*, 38(3), 355–385. <https://doi.org/10.1002/rob.21991>
- Franchi, M., Ridolfi, A., & Pagliai, M. (2020). A forward-looking SONAR and dynamic model-based AUV navigation strategy: Preliminary validation with FeelHippo AUV. *Ocean Engineering*, 196, 106770.
- Franchi, M., Ridolfi, A., & Zacchini, L. (2018). A forward-looking sonar-based system for underwater mosaicing and acoustic odometry. In *2018 IEEE/OES Autonomous Underwater Vehicle Workshop (AUV)* (pp. 1–6).
- Galceran, E., Campos, R., Palomeras, N., Carreras, M., & Ridao, P. (2014). Coverage path planning with realtime replanning for inspection of 3D underwater structures. In *2014 IEEE International Conference on Robotics and Automation (ICRA)* (pp. 6586–6591).
- Galceran, E., & Carreras, M. (2013). A survey on coverage path planning for robotics. *Robotics and Autonomous Systems*, 61(12), 1258–1276.
- Guerneve, T., Subr, K., & Petillot, Y. (2018). Three-dimensional reconstruction of underwater objects using wide-aperture imaging SONAR. *Journal of Field Robotics*, 35(6), 890–905.
- Heng, L., Honegger, D., Lee, G. H., Meier, L., Tanskanen, P., Fraundorfer, F., & Pollefeys, M. (2014). Autonomous visual mapping and exploration with a micro aerial vehicle. *Journal of Field Robotics*, 31(4), 654–675.
- Henson, B. T., & Zakharov, Y. V. (2018). Attitude-trajectory estimation for forward-looking multibeam SONAR based on acoustic image registration. *IEEE Journal of Oceanic Engineering*, 44(3), 753–766.
- Hernández, E., Ridao, P., Mallios, A., & Carreras, M. (2009). Occupancy grid mapping in an underwater structured environment. *IFAC Proceedings Volumes*, 42(18), 286–291.
- Hernández, J. D., Vidal, E., Moll, M., Palomeras, N., Carreras, M., & Kavraki, L. E. (2019). Online motion planning for unexplored

- underwater environments using autonomous underwater vehicles. *Journal of Field Robotics*, 36(2), 370–396.
- Ho, B.-J., Sodhi, P., Teixeira, P., Hsiao, M., Kusnur, T., & Kaess, M. (2018). Virtual occupancy grid map for submap-based pose graph SLAM and planning in 3D environments. In *2018 IEEE/RSJ International Conference on Intelligent Robots and Systems (IROS)* (pp. 2175–2182).
- Hornung, A., Wurm, K. M., Bennewitz, M., Stachniss, C., & Burgard, W. (2013). OctoMap: An efficient probabilistic 3D mapping framework based on octrees. *Autonomous Robots*, 34(3), 189–206.
- Huang, T. A., & Kaess, M. (2015). Towards acoustic structure from motion for imaging sonar. In *2015 IEEE/RSJ International Conference on Intelligent Robots and Systems (IROS)* (pp. 758–765).
- Hurtós, N., Nagappa, S., Cufí, X., Petillot, Y., & Salvi, J. (2013). Evaluation of registration methods on two-dimensional forward-looking SONAR imagery. In *Proceedings of OCEANS'13 MTS/IEEE BERGEN, Bergen (NO)* (pp. 1–8).
- Hurtós, N., Ribas, D., Cufí, X., Petillot, Y., & Salvi, J. (2015). Fourier-based registration for robust forward-looking SONAR mosaicing in low-visibility underwater environments. *Journal of Field Robotics*, 32(1), 123–151.
- Isler, S., Sabzevari, R., Delmerico, J., & Scaramuzza, D. (2016). An information gain formulation for active volumetric 3D reconstruction. In *2016 IEEE International Conference on Robotics and Automation (ICRA)* (pp. 3477–3484).
- Jin, L., Liang, H., & Yang, C. (2019). Accurate underwater ATR in forward-looking sonar imagery using deep convolutional neural networks. *IEEE Access*, 7, 125522–125531.
- Johnson-Roberson, M., Bryson, M., Friedman, A., Pizarro, O., Troni, G., Ozog, P., & Henderson, J. C. (2017). High-resolution underwater robotic vision-based mapping and three-dimensional reconstruction for archaeology. *Journal of Field Robotics*, 34(4), 625–643.
- Kanungo, T., Mount, D. M., Netanyahu, N. S., Piatko, C. D., Silverman, R., & Wu, A. Y. (2002). An efficient k-means clustering algorithm: Analysis and implementation. *IEEE Transactions on Pattern Analysis and Machine Intelligence*, 24(7), 881–892.
- Karaman, S., & Frazzoli, E. (2011). Sampling-based algorithms for optimal motion planning. *The International Journal of Robotics Research*, 30(7), 846–894.
- Karimanzira, D., Jacobi, M., Pfützenreuter, T., Rauschenbach, T., Eichhorn, M., Taubert, R., & Ament, C. (2014). First testing of an AUV mission planning and guidance system for water quality monitoring and fish behavior observation in net cage fish farming. *Information Processing in Agriculture*, 1(2), 131–140.
- Kim, B., Cho, H., Joe, H., & Yu, S.-C. (2018). Optimal strategy for seabed 3D mapping of AUV based on imaging SONAR. In *2018 OCEANS-MTS/IEEE Kobe Techno-Oceans (OTO)* (pp. 1–5).
- Kim, B., Kim, J., Cho, H., Kim, J., & Yu, S.-C. (2019). AUV-based multi-view scanning method for 3-D reconstruction of underwater object using forward scan SONAR. *IEEE Sensors Journal*, 20(3), 1592–1606.
- Kriegel, S., Rink, C., Bodenmüller, T., & Suppa, M. (2015). Efficient next-best-scan planning for autonomous 3D surface reconstruction of unknown objects. *Journal of Real-Time Image Processing*, 10(4), 611–631.
- Larroque, C., de Lépinay, B. M., & Migeon, S. (2011). Morphotectonic and fault-earthquake relationships along the northern ligurian margin (western mediterranean) based on high resolution, multibeam bathymetry and multichannel seismic-reflection profiles. *Marine Geophysical Research*, 32(1–2), 163–179.
- Lee, Y.-D. E., & “Tony” George, R. A. (2004). High-resolution geological AUV survey results across a portion of the eastern Sigsbee Escarpment. *AAPG Bulletin*, 88(6), 747–764.
- Levin, D. (2004). Mesh-independent surface interpolation. In Brunnett, G., Hamann, B., Müller, H., & Linsen, L. (Eds.), *Geometric modeling for scientific visualization* (pp. 37–49). Springer.
- Li, J., Kaess, M., Eustice, R. M., & Johnson-Roberson, M. (2018). Pose-graph SLAM using forward-looking sonar. *IEEE Robotics and Automation Letters*, 3(3), 2330–2337.
- Li, Y., Littlefield, Z., & Bekris, K. E. (2016). Asymptotically optimal sampling-based kinodynamic planning. *The International Journal of Robotics Research*, 35(5), 528–564.
- Mai, N. T., Woo, H., Ji, Y., Tamura, Y., Yamashita, A., & Asama, H. (2017). 3-D reconstruction of underwater object based on extended Kalman filter by using acoustic camera images. *IFAC-PapersOnLine*, 50(1), 1043–1049.
- Manhães, M. M. M., Scherer, S. A., Voss, M., Douat, L. R., & Rauschenbach, T. (2016). UUV Simulator: A Gazebo-based package for underwater intervention and multi-robot simulation. In *OCEANS 2016 MTS/IEEE Monterey*. <https://doi.org/10.1109/oceans.2016.7761080>
- Massot-Campos, M., & Oliver-Codina, G. (2015). Optical sensors and methods for underwater 3D reconstruction. *Sensors*, 15(12), 31525–31557.
- Mitchell, G. A., Orange, D. L., Gharib, J. J., & Kennedy, P. (2018). Improved detection and mapping of deepwater hydrocarbon seeps: Optimizing multibeam echosounder seafloor backscatter acquisition and processing techniques. *Marine Geophysical Research*, 39(1), 323–347.
- Moline, M. A., Woodruff, D. L., & Evans, N. R. (2007). Optical delineation of benthic habitat using an autonomous underwater vehicle. *Journal of Field Robotics*, 24(6), 461–471.
- Moravec, H. P. (1989). Sensor fusion in certainty grids for mobile robots. In *Sensor devices and systems for robotics* (pp. 253–276). Springer.
- Moravec, H. P., & Elfes, A. (1985). High resolution maps from wide angle SONAR. In *Proceedings of the 1985 IEEE International Conference on Robotics and Automation* (Vol. 2, pp. 116–121).
- Negahdaripour, S. (2013). On 3-D motion estimation from feature tracks in 2-D FS SONAR video. *IEEE Transactions on Robotics*, 29(4), 1016–1030.
- OpenCV. (2020). Official website of the OpenCV library. Accessed December 2020. <https://opencv.org/>
- Ozog, P., Troni, G., Kaess, M., Eustice, R. M., & Johnson-Roberson, M. (2015). Building 3D mosaics from an autonomous underwater vehicle, Doppler velocity log, and 2D imaging SONAR. In *2015 IEEE International Conference on Robotics and Automation (ICRA), Seattle, WA (USA)* (pp. 1137–1143).
- Pairet, E., Hernandez, J. D., Carreras, M., Petillot, Y., & Lahijanian, M. (2021). Online mapping and motion planning under uncertainty for safe navigation in unknown environments. *IEEE Transactions on Automation Science and Engineering*, 1–23. <http://doi.org/10.1109/tase.2021.3118737>
- Palomer, A., Ridao, P., & Ribas, D. (2019). Inspection of an underwater structure using point-cloud SLAM with an AUV and a laser scanner. *Journal of Field Robotics*, 36(8), 1333–1344.
- Palomeras, N., Hurtós, N., Carreras, M., & Ridao, P. (2018). Autonomous mapping of underwater 3-D structures: From view planning to execution. *IEEE Robotics and Automation Letters*, 3(3), 1965–1971.
- Papachristos, C., Khattak, S., & Alexis, K. (2017). Uncertainty-aware receding horizon exploration and mapping using aerial robots. In *2017 IEEE International Conference on Robotics and Automation (ICRA)* (pp. 4568–4575).
- Paull, L., Saeedi, S., Seto, M., & Li, H. (2012). Sensor-driven online coverage planning for autonomous underwater vehicles. *IEEE/ASME Transactions on Mechatronics*, 18(6), 1827–1838.
- PCL. (2020). Official website of the PCL library. Accessed December 2020. <https://pointclouds.org/>
- Quigley, M., Conley, K., Gerkey, B., Faust, J., Foote, T., Leibs, J., Wheeler, R., & Ng, A. Y. (2009). ROS: An open-source robot operating system. In *ICRA Workshop on Open Source Software* (Vol. 3, pp. 5).

- Ribas, D., Ridao, P., & Neira, J. (2010). *Underwater SLAM for structured environments using an imaging sonar* (Vol. 65). Springer.
- Rusu, R. B., & Cousins, S. (2011). 3D is here: Point cloud library (PCL). In *2011 IEEE International Conference on Robotics and Automation* (pp. 1–4).
- Schrottke, K., Becker, M., Bartholomä, A., Flemming, B. W., & Hebbeln, D. (2006). Fluid mud dynamics in the wester estuary turbidity zone tracked by high-resolution side-scan sonar and parametric sub-bottom profiler. *Geo-Marine Letters*, *26*(3), 185–198.
- Shin, Y.-S., Lee, Y., Choi, H.-T., & Kim, A. (2015). Bundle adjustment from sonar images and SLAM application for seafloor mapping. In *OCEANS 2015-MTS/IEEE Washington* (pp. 1–6).
- Sodhi, P., Ho, B.-J., & Kaess, M. (2019). Online and consistent occupancy grid mapping for planning in unknown environments. In *2019 IEEE/RSJ International Conference on Intelligent Robots and Systems (IROS)* (pp. 7879–7886).
- Solis, F. J., & Wets, R. J.-B. (1981). Minimization by random search techniques. *Mathematics of Operations Research*, *6*(1), 19–30.
- Şucan, I. A., Moll, M., & Kavraki, L. E. (2012). The open motion planning library. *IEEE Robotics & Automation Magazine*, *19*(4), 72–82. <https://doi.org/10.1109/MRA.2012.2205651>
- Teixeira, P. V., Kaess, M., Hover, F. S., & Leonard, J. J. (2016). Underwater inspection using SONAR-based volumetric submaps. In *2016 IEEE/RSJ International Conference on Intelligent Robots and Systems (IROS)* (pp. 4288–4295).
- Terracciano, D., Bazzarello, L., Caiti, A., Costanzi, R., & Manzari, V. (2020). Marine robots for underwater surveillance. *Current Robotics Reports*, *1*, 159–167.
- Törn, A., & Žilinskis, A. (1989). *Global optimization* (Vol. 350). Springer.
- Turner, J. A., Babcock, R. C., Hovey, R., & Kendrick, G. A. (2018). AUV-based classification of benthic communities of the Ningaloo shelf and mesophotic areas. *Coral Reefs*, *37*(3), 763–778.
- Valdenegro-Toro, M. (2016). Object recognition in forward-looking SONAR images with convolutional neural networks. In *Proceedings of the OCEANS'16 MTS/IEEE MONTEREY, Monterey, CA (USA)*.
- Valdenegro-Toro, M. (2017). Best practices in convolutional networks for Forward-Looking SONAR image recognition. In *Proceedings of the OCEANS'16 MTS/IEEE ABERDEEN, Aberdeen (UK)*.
- Vasquez-Gomez, J. I., Sucar, L. E., & Murrieta-Cid, R. (2014). View planning for 3D object reconstruction with a mobile manipulator robot. In *2014 IEEE/RSJ International Conference on Intelligent Robots and Systems* (pp. 4227–4233).
- Vidal, E., Palomeras, N., Istenič, K., Gracias, N., & Carreras, M. (2020). Multisensor online 3D view planning for autonomous underwater exploration. *Journal of Field Robotics*, *37*(6), 1123–1147.
- Wang, J., Shan, T., & Englot, B. (2019). Underwater terrain reconstruction from forward-looking sonar imagery. In *2019 International Conference on Robotics and Automation (ICRA)* (pp. 3471–3477).
- Wang, Y., Ji, Y., Woo, H., Tamura, Y., Yamashita, A., & Asama, H. (2019). Three-dimensional underwater environment reconstruction with graph optimization using acoustic camera. In *2019 IEEE/SICE International Symposium on System Integration (SII)* (pp. 28–33).
- Wang, Y., Ji, Y., Woo, H., Tamura, Y., Yamashita, A., & Hajime, A. (2018). 3D Occupancy mapping framework based on acoustic camera in underwater environment. *IFAC-PapersOnLine*, *51*(22), 324–330. <https://doi.org/10.1016/j.ifacol.2018.11.562>
- Westman, E., Gkioulekas, I., & Kaess, M. (2020). A volumetric albedo framework for 3D imaging sonar reconstruction. *Imaging*, *15*, 29.
- Westman, E., & Kaess, M. (2019b). Wide aperture imaging SONAR reconstruction using generative models. In *2019 IEEE/RSJ International Conference on Intelligent Robots and Systems (IROS)* (pp. 8067–8074).
- Westman, E., & Kaess, M. (2020). Degeneracy-aware imaging sonar simultaneous localization and mapping. *IEEE Journal of Oceanic Engineering*, *45*(4), 1280–1294. <https://doi.org/10.1109/joe.2019.2937946>
- Williams, D. P., Baralli, F., Micheli, M., & Vasoli, S. (2016). Adaptive underwater sonar surveys in the presence of strong currents. In *2016 IEEE International Conference on Robotics and Automation (ICRA)* (pp. 2604–2611).
- Wynn, R. B., Huvenne, V. A., Le Bas, T. P., Murton, B. J., Connelly, D. P., Bett, B. J., Ruhl, H. A., Morris, K. J., Peakall, J., Parsons, D. R., Sumner, E. J., Darby, S. E., Dorrell, R. M., & Hunt, J. E. (2014). Autonomous Underwater Vehicles (AUVs): Their past, present and future contributions to the advancement of marine geoscience. *Marine Geology*, *352*, 451–468.
- Yguel, M., Aycard, O., & Laugier, C. (2008). Update policy of dense maps: Efficient algorithms and sparse representation. In Laugier, C., & Siegwart, R. (Eds.), *Field and service robotics* (pp. 23–33). Springer.
- Youakim, D., Cieslak, P., Dornbush, A., Palomer, A., Ridao, P., & Likhachev, M. (2020). Multirepresentation, multiheuristic A* search-based motion planning for a free-floating underwater vehicle-manipulator system in unknown environment. *Journal of Field Robotics*, *37*(6), 925–950.
- Zabinsky, Z. B. (2013). *Stochastic adaptive search for global optimization* (Vol. 72). Springer Science & Business Media.
- Zacchini, L., Calabrò, V., Candeloro, M., Fanelli, F., Ridolfi, A., & Dukan, F. (2020). Novel noncontinuous carousel approaches for MEMS-based north seeking using Kalman filter: Theory, simulations, and preliminary experimental evaluation. *IEEE/ASME Transactions on Mechatronics*, *25*(5), 2437–2448.
- Zacchini, L., Franchi, M., Manzari, V., Pagliai, M., Secciani, N., Topini, A., Stifani, M., & Ridolfi, A. (2020). Forward-looking sonar CNN-based automatic target recognition: An experimental campaign with FeelHippo AUV. In *2020 IEEE/OES Autonomous Underwater Vehicles Symposium (AUV)* (pp. 1–6).
- Zacchini, L., Ridolfi, A., & Allotta, B. (2020). Receding-horizon sampling-based sensor-driven coverage planning strategy for AUV seabed inspections. In *2020 IEEE/OES Autonomous Underwater Vehicles Symposium (AUV)* (pp. 1–6).
- Zacchini, L., Ridolfi, A., Topini, A., Secciani, N., Bucci, A., Topini, E., & Allotta, B. (2020). Deep learning for on-board AUV automatic target recognition for optical and acoustic imagery. *IFAC-PapersOnLine*, *53*(2), 14589–14594. <https://doi.org/10.1016/j.ifacol.2020.12.1466>

How to cite this article: Zacchini, L., Franchi, M., & Ridolfi, A. (2022). Sensor-driven autonomous underwater inspections: A receding-horizon RRT-based view planning solution for AUVs. *Journal of Field Robotics*, 1–29. <https://doi.org/10.1002/rob.22061>